An Experimental Study of Porous Mediums on Heat Transfer Characteristics Subjected to Water Jet Impingement

by
William A. Bevan

Submitted in Partial Fulfillment of the Requirements
for the Degree of
Master of Science in Engineering
in the
Mechanical Engineering
Program

YOUNGSTOWN STATE UNIVERSITY
December, 2022

An Experimental Study of Porous Mediums on Heat Transfer Characteristics Subjected to Water Jet Impingement

William A. Bevan

I hereby release this thesis to the public. I understand that this thesis will be made available from the OhioLINK ETD Center and the Maag Library Circulation Desk for public access. I also authorize the University or other individuals to make copies of this thesis as needed for scholarly research.

Signature:

William A. Bevan, Student Date

Approvals:

Dr. Kyosung Choo, Thesis Advisor Date

Dr. Jae Joong Ryu, Committee Member Date

Dr. Stefan Moldovan, Committee Member Date

Dr. Salvatore A. Sanders, Dean of Graduate Studies Date

Abstract

Heat transfer enhancement studies were conducted on two main research areas in heat transfer. Those areas are fluid jet impingement and the use of porous mediums. Fluid jet impingement is a common heat transfer application in industry and is widely studied in research due to the high heat and mass transfer they provide. Porous mediums are another common engineering application that is typically found in heat exchangers and heat pipes due to the high heat transfer coefficient they produce. However, not much research stems from the combination of the two applications.

By combining these two heat transfer applications, experiments were broken into two categories, non-boiling and boiling. Here, an apparatus was fabricated that allowed for both categories to be studied while allowing an inclination toward experimental plausibility. For the non-boiling experiment, flow rates were chosen that ranged from $4{,}000 \leq Re_w \leq 11{,}000$ under both free surface and submerged impinging jets. The goal was to determine the Nusselt number and compare the forced convection effect to the plain surface and porous mediums, i.e., monolayer wick and columnar post wick. Also, the variation in the Nusselt number was determined during lateral nozzle movement. The problems faced in pool boiling are the limited critical heat flux (CHF) and heat transfer coefficient (HTC) caused by the phase change over the heated surface. By employing the monolayer wick and columnar post wick, a decrease in the hydrodynamic instability (Rayleigh-Taylor) wavelength can occur, which provides heat transfer enhancements. To see if further heat transfer enhancements can be obtained, an impinging jet was added to the boiling apparatus with working flow rates of $800 \leq Re_w \leq 1{,}700$.

Results for the non-boiling experiment show that the plain surface outperforms both monolayer wick and columnar post wick. This is due to the flow resistance present in both porous mediums. The rough surface of the monolayer wick saw a drop in the convection effect which was influenced by this flow resistance. The columnar post wick saw a further reduction in the convection effect due to the post's tight pitch distance, l_p=1 mm. This was present in both free surface and submerged impinging jets. The boiling results showed a significant increase in CHF enhancements when the monolayer wick and columnar post wick were employed in the pool boiling setup. This is due to the reduced hydrodynamic instability wavelength, which reduced the vapor generation and delayed surface dry-out. CHF enhancements were further increased by employing an impinging jet. With the combination of the reduced hydrodynamic instability wavelength and impinging jet at the highest flow rate, the plain surface, monolayer wick, and columnar post wick saw an increase of 323.1%, 244.3%, and 266.6%, respectively, in CHF measurements when compared to the basic pool-boiling experiment.

Acknowledgments

First of all, I want to thank my thesis adviser, Dr. Choo. The time in your lab has been rewarding, educational, and influential. I appreciate all the time, consideration, advice, and work you put into helping me with my graduate studies. I would also like to thank my thesis committee members, Dr. Ryu and Dr. Moldovan. Thank you both for your guidance and assistance during my graduate studies. I would also like to thank all the faculty of the Mechanical Engineering department at YSU.

Second, I would like to thank the Graduate School and Mechanical Engineering department for granting me a Graduate Assistantship during my first semester of graduate school. I would also like to thank the Cushwa/Commerical Shearing Graduate Fellowship for funding me through the rest of my graduate studies. Thank you to both for giving me the opportunity to advance my knowledge in mechanical engineering while acquiring practical research skills.

Lastly, I would like to thank my family for their constant support throughout my graduate career. I would also like to thank my cats, Moo and Benny, and my dogs, Nova and Shep, for keeping me company while I wrote.

Contents

List of Figures

List of Tables

Nomenclature

Variables

λ	Instability Wavelength
$\dot{q}_{boiling}$	Boiling Heat Flux
$\dot{q}_{nucleate}$	Nucleate Boiling Heat Flux
u	Fluid Velocity
T	Temperature
l	Length
C	Celcius
OD	Outer Diameter
ID	Inner Diameter
t	Thickness
r	Radial Variation
H	Nozzle Height
d	Diameter of Nozzle
Nu	Nusselt Number
Re	Reynolds Number
Pr	Prandtl Number

L	Liters
cc	Cubic Centimeters
mm	millimeters
cm	centimeters
W	Watts
μ	Viscosity
h	Enthalpy
g	Gravitational Acceleration
ρ	Density
σ	Surface Tension of Liquid-Vapor Interface
c_p	Specific Heat
C_{sf}	Experimental Constant that Depends on Surface-Fluid
C	Experimental Constant Based on Heater Geometry
R	Thermal Resistance
$\dot{Q}$	Heat Transfer Rate
Y	Mass Fraction
J	Diffusional Mass Flux
δ	Unit Tensor
τ	Viscous Stress Tensor
E	Total Energy
p	Pressure

P	Normalized Pressure
ϵ	Porosity
y	Distance normal to the Wall
D	Fictitious Down Stream Drag Force
β_j	Radius at Which Hydraulic Jump Begin
β_ζ	Radius at Subcritical Depth
β_η	Radius at Supercritical Depth
F_β	Froude Number
F_{β_ζ}	Subcritical film Froude Number
F_{β_η}	Supercritical film Froude Number
a	Value of Data Set
b	Mean of Data Set
N	Total Number of Data Points

Subscripts

ps	Plain Surface
m	Monolayer
cp	Columnar Post
u	Uniform
l	Liquid
v	Vapor

p	Pitch Distance
$stag$	Stagnation Point
fg	Vaporization
s	Surface
sat	Saturation
r	Radial Variation
c	Contact Resistance
∞	Ambient Temperature
$Cond$	Conduction Heat Transfer
$Conv$	Convection Heat Transfer
Min	Minimum Boiling Heat Flux
Max	Maximum Boiling Heat Flux
$Film$	Film Boiling Heat Flux
cr	Critical Heat Flux Constant
br	Breakthrough Bubble
j	Hydraulic Jump
ζ	Liquid Sheet Thickness After Hydraulic Jump
η	Local Thickness of Liquid Sheet

Superscripts

n	Experimental Constant that Depends on the Fluid
*	Normalized Value

Acronyms

CHF	Critical Heat Transfer
HTC	Heat Transfer Coefficient
RT	Rayleigh-Taylor
CAD	Computer-Aided Design
PTFE	Polytetrafluoroethylene
HCTB	Hot Circulating Temperature Bath
EV	Electric Vehicles
SD	Standard Deviation
SE	Standard Error

Chapter 1. Introduction

1.1 Problem Statement

Heat transfer enhancements are a popular research area and are even more popular now due to technological advancements. For example, advancements in electronics (cell phones and computers), electric vehicles (EVs), and everyday appliances all require optimal heat transfer applications to keep the products in operation. An impinging jet is ideal for an application that requires cooling, heating, or drying. Impinging jets are commonly used in heat transfer applications due to their high rates of heat and mass transfer [1, 9, 67-78]. Common applications of impinging jets include turbine blade cooling and electronics equipment cooling. Another heat transfer application used for its increase in HTC is porous mediums. Porous mediums are typically found in heat exchangers and heat pipes due to the increase in heat transfer they provide [2-8, 10-66]. The combination of jet impingement and porous media could provide optimal heat transfer enhancements if used correctly in conjunction with each other.

This thesis will explore the combination of a single-phase impinging jet and porous mediums in hopes of seeing heat transfer enhancements. Results will investigate the cases of a non-boiling experiment and a boiling experiment. Motivations behind this research are centered around previous research of impinging jets and porous mediums, but no recent research shows them in conjunction with each other. With the combination of jet impingement and porous mediums, conclusions will be drawn about the convection effect on the different porous materials for the non-boiling case. For the non-boiling case, working Reynolds numbers in the range of $4{,}000 \leq Re_w \leq 11{,}000$ were chosen in which the plain surface and porous mediums will be exposed to a free surface and submerged impinging jet. For the boiling case, Reynolds numbers of $0 \leq Re_w \leq 1{,}700$ were chosen in which the plain surface and porous mediums will be under a submerged jet only, to replicate the pool-boiling effect. Conclusions will be centered around the HTC, CHF, and the reduction in the excess temperature. Details on the selected Reynolds numbers will be further discussed throughout this report

Chapter 2. Background

2.1 Heat Transfer

Heat transfer and thermodynamics go hand in hand in the field of thermal engineering. While the study of thermodynamics does not mention how long a process will take; rather, it concerns the quantity of heat transfer when a system transitions from one equilibrium state to another. In many advanced thermal engineering applications, engineers are often interested in the rate of heat transfer. This rate-based analysis is the science of heat transfer. The field of heat transfer is broken into three primary mechanisms, which are conduction, convection, and radiation. This thesis will focus on the first two primary mechanisms, conduction, and convection.

2.1.1 Conduction

Conduction is the process by which energy is transferred from the more energetic particles to the nearby, less energetic ones through interactions between the particles of a substance. The conduction phenomenon can take place in solids, liquids, and gases. Conduction occurs in gases and liquids as a result of molecule collisions and diffusion during random molecular motion. In solid materials, it results from the interaction of the free electron transit of energy and the vibrations of the molecules in a lattice. The geometry, thickness, and material of a medium, as well as the temperature differential across the medium, all affect the rate of heat conduction across it. Heat conduction can be modeled by an equation developed by Joseph Fourier in 1822 in his book entitled "The Analytical Theory of Heat" [11]. Equation 2.1 shows Fourier's law of heat conduction.

$$\dot{Q}_{cond} = -kA\frac{dT}{dx} \tag{2.1}$$

Presented in Equation 2.1, dT/dx is the temperature gradient, k is the thermal conductivity, and A is the area. When the temperature falls with an increase in x, heat is transported in the direction of the falling temperature, and the temperature gradient turns negative. The negative sign in Equation 2.1 ensures that heat transfer in the positive x-direction is a positive quantity. A more general form of the heat conduction equation is presented in Equation 2.2. Here, Equation 2.2 accounts for rectangular space coordinates and variable thermal conductivity.

$$\frac{\partial}{\partial x}\left(k\frac{\partial T}{\partial x}\right)+\frac{\partial}{\partial y}\left(k\frac{\partial T}{\partial y}\right)+\frac{\partial}{\partial z}\left(k\frac{\partial T}{\partial z}\right)+\dot{e}_{gen}=\rho c\frac{\partial T}{\partial t} \tag{2.2}$$

It is seen in Equation 2.2 that the general heat conduction equation is time-dependent. By factoring out the transient state of Equation 2.2 and simplifying it down to a one-dimensional case, the heat conduction equation takes on the form of Equation 2.3. Equation 2.3 is the steady-state one-dimensional heat conduction equation.

$$\dot{Q}_{cond}=kA\frac{T_1-T_2}{\Delta x} \tag{2.3}$$

2.1.2 Convection

Another heat transfer mechanism is convection. Convection is the mechanism of heat transfer through a fluid in the presence of bulk fluid motion [2]. Depending on how the fluid motion is started, convection can be either natural (or free) or forced. In forced convection, the fluid is propelled externally, such as by a pump or a fan, across a surface or via a conduit. Any fluid motion in natural convection is brought about by organic processes like the buoyancy effect, which appears as the rise of warmer fluid and the fall of colder fluid. Depending on whether a fluid is pushed to flow within a pipe or across a surface, convection can also be classified as external or internal. Experimental work has shown that the fluid parameters of dynamic viscosity μ, thermal conductivity k, density ρ, specific heat c_p, and fluid velocity u all have a significant impact on convection heat transfer [1, 9, 67-78]. Along with the kind of fluid flow, it also depends on the geometry and roughness of the solid surface (such as being streamlined or turbulent). As a result of convection's dependency on so many factors, it is anticipated that the heat transfer relations resulting from convection will be highly complicated. According to Newton's rule of cooling, the rate of convection heat transfer is readily represented as a function of the temperature difference. It is expressed in Equation 2.5 with h as the heat transfer

coefficient, A_s as the heat transfer surface area, T_s as the surface temperature, and T_∞ as the temperature of the fluid sufficiently far from the surface.

$$\dot{Q}_{conv} = hA_s(T_s - T_\infty) \tag{2.4}$$

The rate of heat transmission between a solid surface and a fluid per unit surface area per unit temperature difference is known as the convection heat transfer coefficient or h. In general, the flow direction determines the variation in the convection heat transfer coefficient. In these situations, the local convection heat transfer coefficients are correctly averaged over the entire surface to produce the average or mean convection heat transfer coefficient for a surface [2].

In order to decrease the total number of variables in convection research, it is usual practice to nondimensionalize the governing equations and combine the variables, which group together into dimensionless numbers. This was done by Wilhelm Nusselt, who derived the dimensionless convection heat transfer coefficient number entitled the Nusselt number. Equation 2.5 shows the Nusselt number equation with h the heat transfer coefficient, L_c the characteristic length, and k_f the thermal conductivity of the working fluid.

$$Nu = \frac{hL_c}{k_f} \tag{2.5}$$

The physical significance of the Nusselt number can be understood by a uniform fluid layer. Convection is used to transmit heat through the fluid layer while the fluid is in motion, and conduction is used when the fluid layer is still. As a result, the Nusselt number describes how much more efficiently heat is transferred through a fluid layer as a result of convection than by conduction. The effectiveness of convection increases with increasing Nusselt number. A fluid layer with a Nusselt number of Nu=1 indicates that heat is transferred across the layer only by conduction [2].

Presented in fluid mechanics is a phenomenon called the velocity boundary layer, which occurs when a fluid flows over a surface. This same type of phenomenon happens in heat transfer which is called the thermal boundary layer. The thermal boundary layer is the flow region over the surface in which the temperature variation in the direction normal to the surface is significant. Figure 2.1 shows a schematic of the thermal boundary layer phenomenon.

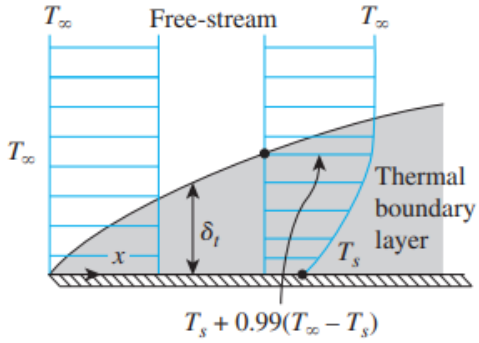

Figure 2.1: Schematic of Thermal Boundary Layer [2].

Describing the thermal boundary layer further is the dimensionless parameter, the Prandtl number named after Ludwig Prandtl. Equation 2.6 shows the Prandtl number equation with μ as viscosity, c_p the specific heat, and k thermal conductivity. The proportion of momentum to thermal diffusivity is known as the Prandtl number. For heat transfer applications, the Prandtl number describes the relative thickness of the momentum and thermal boundary layers.

$$Pr = \frac{\mu c_p}{k} \tag{2.6}$$

Another major part of convection heat transfer is the characterization of the different flow regimes. Flow regimes can be broken into three classes, laminar, transition, and turbulent flows. Laminar flow is characterized by a smooth flow field and highly ordered motion. Turbulent flow is characterized by velocity fluctuations and highly-disordered motion. The transition region falls between laminar and turbulent flows. The transition period from laminar to turbulent is not a sudden occurrence; rather, it occurs over some region in which the flow fluctuates from laminar to turbulent. Most engineering applications encounter turbulent flows due to the demand for high-velocity applications.

Laminar to turbulent flow transitions are influenced by a variety of factors, including fluid type, flow velocity, surface temperature, and surface geometry. Osborn Reynolds, a fluid dynamics researcher, observed that the flow regime depends mainly on the ratio of the inertia forces to viscous forces in the fluid. This ratio is called the Reynolds number. Equation 2.7 shows the Reynolds number with ρ as density, u as the fluid velocity, L_c as the characteristic length, and μ as the viscosity.

$$Re = \frac{\rho u L_c}{\mu} \tag{2.7}$$

Since the inertia forces are more significant than the viscous forces at high Reynolds numbers and are related to the fluid's density and velocity, the viscous forces are unable to stop the fluid's random and rapid oscillations. However, for low or moderate Reynolds numbers, the viscous forces are sufficient to overcome these variations and maintain the fluid's "linearity." As a result, in the first scenario, the flow is turbulent, whereas, in the second, it is laminar. The critical Reynolds number is the Reynolds number at which the flow starts to get turbulent. The critical Reynolds number varies depending on the geometry and flow conditions. The amount of turbulence in the free stream, however, may have a significant impact on the critical Reynolds number value.

2.2 Pool-Boiling

Boiling is a phenomenon that happens when a liquid is brought into contact with a surface that is kept at a temperature T_s that is sufficiently higher than the liquid's saturation temperature T_{sat} at the solid-liquid interface. The result is a liquid-to-vapor phase change process. At the solid-liquid interface, vapor bubbles quickly develop during the boiling process. When these bubbles reach a specific size, they separate from the surface and make an effort to ascend to the liquid's free surface. Due to the numerous factors that must be considered during the process, as well as the intricate fluid motion patterns brought on by the development and expansion of bubbles, boiling is a problematic event [14]. Figure 2.2 shows a schematic of the boiling phenomenon.

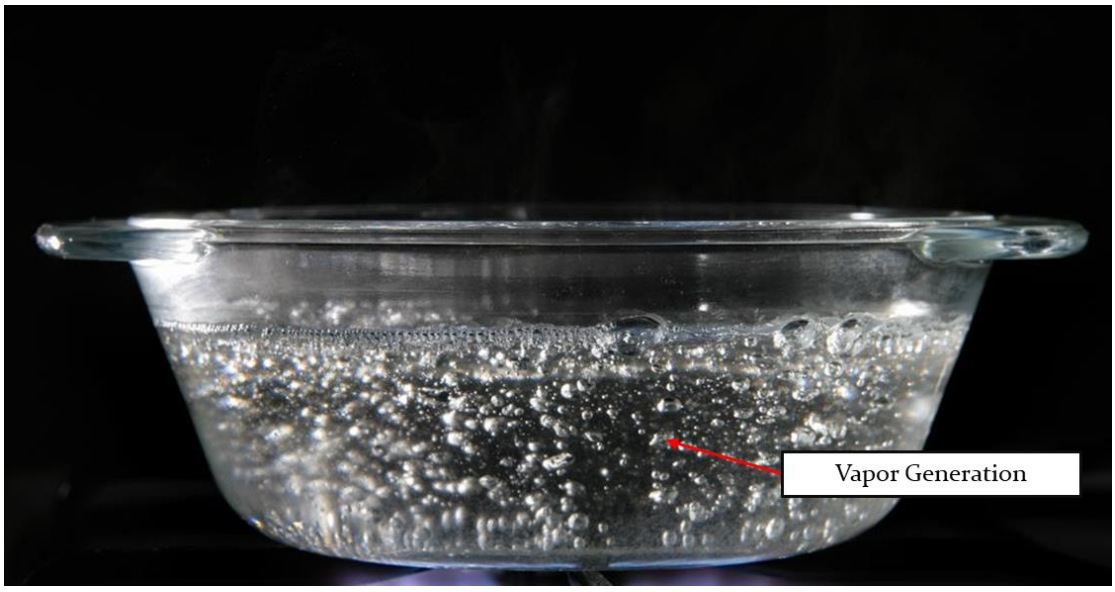

Figure 2.2: Depiction of Pool Boiling Phenomenon [15].

The boiling heat flux, $\dot{q}_{boiling}$, from a solid surface to the fluid is described by Newton's law of cooling as a type of convection heat transfer which is expressed in Equation 2.8. Presented in Equation 2.8 is h, the heat transfer coefficient, and $\Delta T_{excess,}$ which is the excess temperature of the surface above the saturation temperature of the fluid.

$$\dot{q}_{boiling} = h\Delta T_{excess} \tag{2.8}$$

The parameters of the liquid or vapor, as well as h_{fg}, the latent heat of vaporization, and σ, the surface tension, are all included in the study of boiling heat transfer. The fundamental amount of energy transmitted during boiling heat transfer is known as the h_{fg}, which is represented as the energy absorbed as a unit mass of liquid vaporizes at a certain temperature or pressure. Due to the attraction force on molecules at the interface toward the liquid phase, surface tension at the liquid-vapor interface is what gives bubbles their ability to form. With the rising temperature, surface tension falls until it reaches zero at the critical point. This explains why boiling at supercritical pressures and temperatures does not produce any bubbles.

Normally, the bubbles are not in thermodynamic equilibrium with the surrounding liquid, and the boiling processes do not occur under equilibrium circumstances. That is, the vapor in a bubble often has a different temperature and pressure than the liquid. The surface tension at the contact equalizes the pressure differential between the liquid and the vapor. Heat transmission between the two phases is fueled by the difference in temperature between the liquid surrounding a bubble's vapor and that liquid. Heat is transmitted from the bubble into the liquid when the liquid is colder than the bubble, which causes part of the vapor inside the bubble to condense and finally causes the bubble to burst. Heat is transmitted from the liquid to the bubble when the liquid is hotter than the bubble, which causes the bubble to expand and rise to the top due to buoyancy.

Boiling is classified as pool-boiling in the absence of bulk fluid flow. During the pool-boiling phenomenon, the fluid body is immobile; any movement of the fluid is brought on by natural convection currents, and the motion of the bubbles is caused by buoyancy. Looking at pool boiling further, it can be classified as subcooled or saturated boiling depending on the bulk liquid temperature. Subcooled boiling happens when the temperature of the main body of the liquid is below saturation temperature [16,17]. In conjunction, saturated boiling happens when the temperature of the liquid is equal to the saturation temperature [18].

Despite being the least understood type of heat transfer, boiling is most likely the most well-known. Though much research has been conducted on pool-boiling, empirical correlations are still used to predict the rate of boiling heat transfer. Shiro Nukiyama has made significant contributions to the study of boiling heat transfer. Nukiyama utilized electrically heated nichrome and platinum wires immersed in liquids to develop four different boiling regimes [2,19]. Those four boiling regimes are natural convection boiling, nucleate boiling, transition boiling, and film boiling. These four boiling regimes for water can be illustrated by a boiling curve which is seen in Figure 2.3. The curve's precise shape is determined by the material combination of the fluid and the heating surface, as well as the fluid pressure. Still, it is essentially unaffected by the heating surface's geometry.

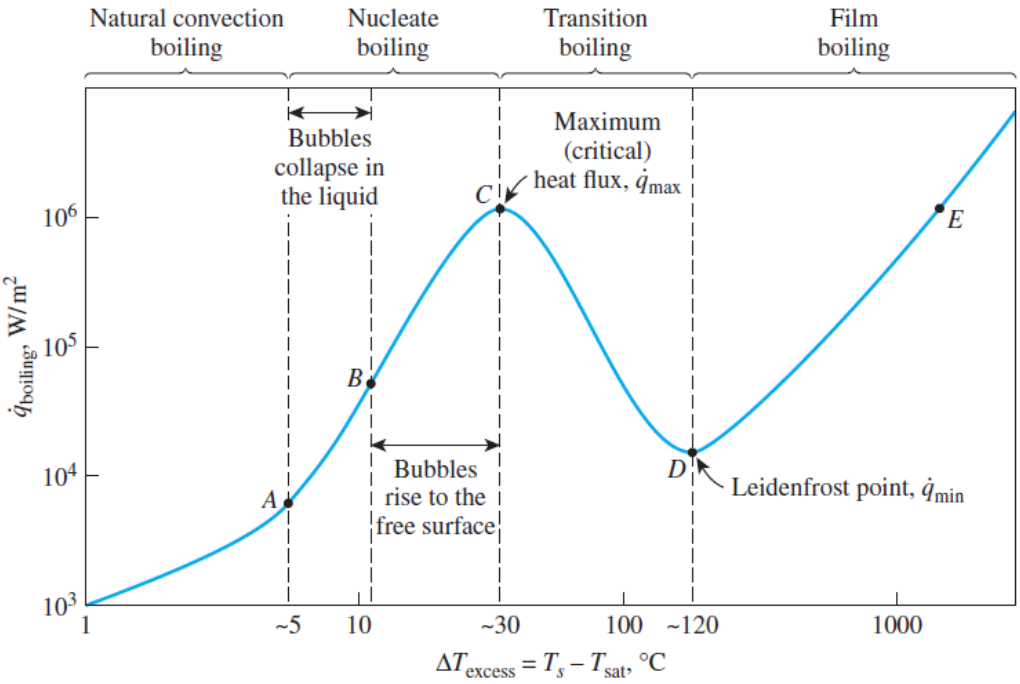

Figure 2.3: Boiling Curve for Water at 1 atm Pressure [2].

The first part of the boiling curve is the natural convection boiling regime. Here, the heated surface temperature is slightly above the saturation temperature. Hence, the liquid is somewhat superheated and evaporates when it rises to the free surface [22]. The smooth movement of natural convection currents controls natural convection boiling, and natural convection transfers heat from the heating surface to the fluid. Heat transfer rates in the natural convection boiling regime can be determined using natural convection relationships.

The next boiling regime consists of nucleate boiling. This is when bubble generation is first noticed in pool-boiling. The nucleate boiling regime can be broken into two different regions. In region A to B, isolated vapor pockets are formed at various preferential nucleation sites on the heated surface. But as soon as they break from the surface, these bubbles disappear in the liquid. The liquid close to the heater surface fills the area left vacant by the rising bubbles, and the process is then repeated. The enhanced heat transfer coefficient and heat flow in this area of nucleate boiling are primarily due to the swirling and agitation brought on by the entrainment of the liquid to the heater surface.

The second region, B to C, surface temperature is increased, and because there are so many nucleation sites, bubbles grow at such high rates that they create several continuous columns of vapor in the liquid. Due to the quick velocity, the bubbles are able to rise to the surface, where they burst and release their vapor content. Many empirical correlations have been conducted in the nucleate boiling regime, though the most popular is that conducted by Warren M. Rohsenow [2,5,6]. The Rohsenow correlation is shown in the results and discussion section of this report as Equation 4.3.

Careful consideration should be taken around point C of the boiling curve. This point is known as the critical heat flux point, $\dot{q}_{max}$. At the CHF point, it is difficult for liquid to reach the heater surface and wet it because the rate of evaporation at the heater surface reaches such high values that a significant portion of it is covered with bubbles. This is called surface dry-out. This CHF value was modeled by both Kutateladza and Zuber using different approaches [20-23]. The correlation is expressed in Equation 2.9. In Equation 2.9 is the value of $C_{cr,}$ which is a constant based on the work of Lienhard dependent on heat geometry [24,25].

$$\dot{q}_{max} = C_{cr} h_{fg} [\sigma g \rho_v^2 (\rho_l - \rho_v)]^{1/4} \tag{2.9}$$

The third boiling regime is called transition boiling. It is present that there is a noticeable drop in heat flux in the transition regime. This is due to the vapor coating that covers a sizable portion of the heater's surface and serves as insulation because vapor has a lower thermal conductivity than liquid does. Nucleate and film boiling both take place in part during the transition boiling regime. This regime is often avoided in practical applications due to the unstableness of the boiling phenomenon.

The last boiling regime is film boiling. Here, an interesting anomaly occurs called the minimum heat flux, $\dot{q}_{min}$. For the minimum heat flux to occur, the heater surface is completely covered by a continuous stable vapor film. This minimum heat flux point is also called the Leidenfrost point, developed by J.C. Leidenfrost in 1756, who observed liquid droplets on a very hot surface jump around and slowly boil away [2]. The minimum heat flux can be modeled by an equation developed by Novak Zuber in 1958. Equation 2.10 shows the minimum heat flux equation. It wasn't until 1961 that P.J. Berensen conducted further experiments for a better empirical correlation of the minimum heat flux equation [26]. Although a relationship is obtained for the minimum heat flux, error can still be 50% or more due to the complications of boiling.

$$\dot{q}_{min} = 0.09\rho_v h_{fg}\left[\frac{\sigma g(\rho_l-\rho_v)}{(\rho_l-\rho_v)^2}\right]^{\frac{1}{4}} \tag{2.10}$$

The film boiling regime can also be modeled by an equation. Bromley, in 1950 established a theory for the prediction of heat flow for stable film boiling on the exterior of a horizontal cylinder using an analysis akin to Nusselt's theory on filmwise condensation [27]. For a horizontal cylinder or sphere of diameter D, the heat flow for film boiling is provided in Equation 2.11.

$$q_{film} = C_{film}\left[\frac{gk_v^3(\rho_l-\rho_v)[h_{fg}+0.4c_{pv}(T_s-T_{sat})]}{\mu_v D(T_s-T_{sat})}\right]^{\frac{1}{4}}(T_s - T_{sat}) \tag{2.11}$$

The relationships that were previously mentioned were all developed for a polished boiling surface. This means that the nucleation sites of vapor generation are on the same sublevel with the fluid contact on the heater surface. These polished surfaces have allowed researchers to develop empirical correlations based on heater properties and geometry. Though these correlations offer a closed-form solution, high levels of error are associated with the equations. This is due to the complications of phase change that happen during boiling. Hence, careful consideration should be taken when using these equations.

2.2.1 Porous Mediums

As stated in the previous section, pool boiling offers a passive high heat flux cooling technology with a minimal temperature gradient. Applications of pool boiling include electronic cooling [28-31], renewable energy systems [32], and operations in energy production [33]. However, the main problem in pool boiling is the limited heat removal capability, also called the critical heat flux (CHF), and the poor heat transfer coefficient (HTC) due to surface dry-out. Surface dry-out is a factor of insufficient liquid supply to the heated surface by the effect of a critical liquid-vapor hydrodynamic wavelength. This hydrodynamic wavelength is also called the Rayleigh-Taylor instability wavelength. When a lighter fluid supports a heavier fluid, Rayleigh-Taylor instability (RT) results. Any disturbance of the interface increases and causes spikes of the heavier fluid to penetrate into the lighter one, causing the interface to become unstable [34].

Developed by Lord Rayleigh and Sir Geoffrey Ingram, the conservation equations between two miscible fluids are described by Equation 2.12 through Equation 2.14. Y is the mass fraction, J is a diffusional mass flux, δ is the unit tensor, τ is the viscous stress tensor, p is pressure, and E is total energy.

$$\frac{\partial \rho Y_i}{\partial t} + \nabla \cdot \left(\rho Y_i \vec{u} + \vec{J_i}\right) = 0; (i = 1, 2, 3 \ldots . n) \tag{2.12}$$

$$\frac{\partial \rho \vec{u}}{\partial t} + \nabla \cdot \left[\rho \vec{u} + p\vec{\delta} - \vec{\tau}\right] = \rho \vec{g} \tag{2.13}$$

$$\frac{\partial E}{\partial t} + \nabla \cdot [(E + p)\vec{u} - \vec{\tau} \cdot \vec{u} + \vec{q}_{cond} + \vec{h}_{fg} = \rho \vec{g} \cdot \vec{u} \tag{2.14}$$

The increased hydrodynamic instability wavelength limits the pool boiling performance; however, this has motivated research efforts to understand surface dry-out and enhance the CHF and HTC, respectively. This is where the research area of porous mediums comes into play. Porous mediums utilize different materials and shapes based on the engineering applications. Typical porous medium materials include copper, ceramics, and other metallics. Shapes of porous mediums include honeycomb structures, microchannels, and mesh-like wicks. Porous materials are typically found in heat exchangers and heat pipes due to the high HTC they produce, which optimizes the heat transfer rate.

By enhancing the liquid supply to the evaporator (or vapor escape from the evaporator), various micro-/nanoscale surface engineering approaches have demonstrated improvements in CHF and/or HTC. These approaches include rough surfaces, random porous matrices, microchannels/grooves, foams, mesh-like wicks, uniform porous coatings, nanostructures, and hybrid micro-/nanostructures [4,7,8,35-54].

Some early research on heat transfer enhancements in pool boiling comes from the work of Chang and You. They conducted pool boiling research on five different porous surfaces in saturated FC-72. Their results showed by employing micro-porous coatings in pool boiling; the enhanced surfaces showed about 80%-90% reduction of the superheat. This superheat reduction led to about 30% enhancement of the nucleate boiling HTC and about 100% enhancement in CHF. These enhancements are directly related to the increased active nucleation site density from the direct visualization [55].

Kim and You also studied heat transfer enhancements from microporous surfaces in saturated FC-72. Their research involved platinum wires coated with synthetic Diamond particles/Omegabond 101 epoxy binder/Methyl-ethyl-keytone (DOM) porous coatings. They concluded that the much larger active nucleation site density of the microporous covering, as opposed to an increase in surface area, directly contributes to its enhanced nucleate boiling heat transfer. They also found that the reduced bubble size, increased departure frequency, and density of active nucleation sites for improved convection heat transfer and favorable hydrodynamic instability changes [56].

Hwang and Kaviany studied various uniform microporous coatings using copper-sintered particles in pool boiling with n-pentane as the working fluid[7]. Based on the CHF equation based on Zuber [23] and with the previous research of Liter and Kaviany [8], Zuber's CHF equation can be modified to include the hydrodynamic instability wavelength, which is shown in Equation 2.15 along with the Rayleigh-Tayler wavelength shown in Equation 2.16.

$$\dot{q}_{max} = \Delta h_{fg} \left(\frac{\pi^3 \sigma \rho_v}{288 \lambda_{RT}} \right)^{\frac{1}{2}} \tag{2.15}$$

$$\lambda_{RT} = 9 \left[\frac{\sigma}{g(\rho_l - \rho_v)} \right]^{\frac{1}{2}} \tag{2.16}$$

With the addition of the copper-sintered particles, a semi-empirical correlation of the CHF has been modeled by Polezhaev and Kovalev, shown in Equation 2.17 [58]. Where d_{br} is the diameter of the breakthrough bubble onset of bubble penetration through a uniform porous coating, and ϵ is the porosity. Hwang and Kaviany concluded that the uniform microporous coatings' enhanced CHF is due to a shorter hydrodynamic instability wavelength, whereas various particle types might alter HTC [7].

$$\dot{q}_{max} = 0.52\epsilon^{2.28}\Delta h_{fg}\left[\frac{2\sigma\rho_l\rho_v}{(\rho_l+\rho_v)d_{br}}\right]^{\frac{1}{2}} \tag{2.17}$$

Gradient metal foam has been studied by Xu and Zhao to reduce the significant fluid resistance characteristic and regulate the desired bubble form [59]. Their results show that by employing a gradient copper-nickel foam with a nanoparticle layer, they were able to control bubble generation. Also, the addition of the nickel fiber with the deposited alumina nanoparticles allowed for better heat transfer from the vapor cloud to the nickel fiber. To analyze how the regulated liquid supply and bubble escape mechanism affect the CHF and HTC, Jaikumar and Kandlikar used microchannels of various sizes (300 μm–762 μm) covered with sintered particles consisting of fin top, channels alone, and full fin surfaces [60]. They concluded their results by saying a broader channel had a greater CHF and HTC than a narrower channel because it had more liquid paths to feed to the nucleation sites in the sintered throughout configuration.

Nonuniform surface engineering techniques have also been used to further enhance the pool's boiling performance. Liter and Kaviany showed that the CHF is three times higher compared to plain surfaces by employing a 3D conical wick structure to manage the dominating bubble nucleate sites through the thin wick and crucial hydrodynamic instability wavelength using the pitch distance of the thick wick [8]. They concluded that the nucleation sites are generated at the heated surface while the conical wicks allowed adequate liquid supply to the evaporator. With their design, CHF enhancements were achieved by further prohibiting surface dry-out of the conical wick. Similarly, Min, Hwang, Usta, Cora, Koc, and Kaviany studied 2-D and 3-D modulated porous coating in pool boiling using n-pentane as the working fluid [61]. They concluded that the 2-D and 3-D modulated porous surfaces behaved similarly in pool boiling. However, they were able to actively control the hydrodynamic instability wavelength, which is the result of CHF enhancements.

Qu, Xu, Zhao, and Tao studied pool boiling heat transfer on horizontal metallic foam surfaces with crossing and single-directional V-shaped grooves in saturated water [62]. They found that an ideal groove volume ratio, which corresponds to the highest heat transfer coefficient for crossed groove ray structure, exists in dependence on pore density. In the heat flux range of $q \leq 1.0*10^5$ W/m^2, the best groove volume ratio was 7.76% and 5.84% for corresponding pore densities of 100 and 130PPI. Similarly, Bai, Zhang, Guo, Lin, Bu, and Wen studied boiling heat transfer characteristics in an artery porous structure [63]. Their goal was to employ an artery porous structure by creating separate flow channels for liquid supply and vapor venting and retaining the liquid/vapor contact inside the porous structure. When compared to a plain surface, they were able to enhance the CHF of nucleate pool boiling. They have also concluded in their work that there is an optimal pore size to achieve the best pool boiling performance.

Much research has also been conducted on the employment of modulated wicks in heat pipes and vapor chambers. Hwang, Kaviany, Anderson, and Zuo studied the performance of modulated wicks in heat pipes [64]. Through experimental research, they were able to increase the HTC in the heat pipes by employing evaporating wicks. Hwang, Nam, Fleming, Dussinger, Ju, and Kaviany also studied multi-artery heat pipe spreader [65]. Their results showed the evaporator wick resistance is smallest at high heat fluxes. This results in an increase in CHF enhancements.

Some of the latest pool boiling research comes from Nasersharifi, Kaviany, and Hwang, who studied pool boiling enhancements using multilevel modulated wicks using n-pentane as the working fluid [4]. They created multi-level modulated wicks, such as monolayer, columnar posts, and mushroom posts, by employing sintered spherical particles to concurrently improve the CHF and HTC. The goals in mind of the researchers was to reduce the Rayleigh-Taylor instability wavelength, λ_m, through the capillary body for enhanced CHF and to also reduce the effective wick thickness for a large HTC. They first started with the monolayer design, which consisted of a single layer of copper-sintered particles that were roughly 200 μm in diameter. The purpose of the monolayer wick is to increase the HTC by decreasing the effective wick thickness. The researchers conducted the effective wick thickness based on the effective HTC, which is particle size dependent via the effective thermal conductivity based on research by Hwang [66]. The CHF enhancements were 20% higher on the monolayer wick when compared to the plain surface. They concluded that this enhancement is directly related to the possible decrease in the hydrodynamic instability wavelength [4, 7]. Based on the work of Kim, Nasersharifi concluded that the monolayer wick increases the HTC and, in comparison to a plain

surface, lowers the superheat at a given heat flux, which is due to the monolayer wick's enhanced effective thermal conductivity [57].

In conjunction with the monolayer wick, Nasersharifi fabricated columnar post wicks by adding a thick columnar post to the monolayer wick. This was done in order to improve CHF and HTC significantly; it is necessary to actively manage (or lower) the Rayleigh-Taylor instability wavelength through the pitch spacing between consecutive columnar posts based on the work of Liter and Min [8, 61]. While the thin monolayer wick is used to improve HTC by reducing conduction resistance to evaporation sites, i.e., the ends of the capillary meniscus on the monolayer wick, the thick columnar wick's main function is to help the liquid supply from the liquid pool via capillary flow. The vapor produces and escapes through the spaces between the columns because the active evaporation sites are found in the liquid meniscus of the monolayer. By introducing the columnar post, the columnar pitch activily modulates the hydrodynamic instability wavelength, as shown in Equation 2.18.

$$\frac{\dot{q}_{max}}{\frac{\pi}{24}\rho_v^{\frac{1}{2}}\Delta h_{fg}[\sigma g(\rho_l-\rho_v)]^{\frac{1}{4}}} = \frac{3\left[\frac{\sigma}{g(\rho_l-\rho_v)}\right]^{\frac{1}{4}}}{\lambda_m^{\frac{1}{2}}} \tag{2.18}$$

Results based on Nasersharifi's research show a columnar pitch distance of 3.5 mm and 1 mm, both showed CHF enhancements when compared to the plain surface in pool boiling. Lastly, Nasersharifi added a mushroom cap to the columnar post-wick structure. Due to the additional surface area the caps give, the mushroom posts make it simpler to provide fluids to the monolayer, which might delay surface dry-out. Additionally, the mushroom caps restrict vapor from departing right away, which encourages evaporation close to the monolayer wick and therefore increases HTC, particularly in the high heat flux regime. Though the mushroom post wick did not perform as well as the columnar post wick, the mushroom post wick assisted the liquid supply to the heated surface and favorably regulated the departure bubble size and departure frequency, which resulted in a better HTC. Conclusions of Nasersharifi's research showed as compared to a plain surface, the monolayer wick improves the CHF by 20%, while the mushroom and columnar posts improve the CHF by 87% and 65%, respectively. These results were obtainable by reducing the hydrodynamic instability wavelength.

2.3 Jet Impingement

Impinging jets offer high rates of heat and mass transfer. Engineering applications of jet impingement include gas turbine cooling, rocket launcher cooling, and high-density electrical equipment cooling [79-81]. Although impinging jets are optimal for cooling, they are also used in heating and drying applications. An impinging jet setup typically includes a nozzle and a heated source. The working fluid can either be water, air, refrigerant, or a combination of fluids. The basic phenomenon of an impinging jet is a high-velocity fluid jet that impinges a heated surface. The result is a thin boundary of fluid on the heated surface that provides optimal heat transfer in the form of convection. There are three common jet impingement configurations. Those configurations are free surface impinging jets, submerged impinging jets, and confined impinging jets.

2.3.1 Free Surface Jet Impingement

To describe a free surface jet, there are no additional boundary conditions on the impinging surface. That is, the fluid of the impinging jet has free behavior. To better describe the behavior of a free surface impinging jet, Figure 2.4 shows a schematic. In Figure 2.4, D is the inner nozzle diameter, and Z or H is the nozzle-to-plate spacing. Upon exit of the nozzle, the fluid is fully developed for pipe flow. During its travel to the impinging surface, the velocity gradient becomes parabolic, with the greatest velocity at the jet center. The direct center of the impinging plate is known as the stagnation point. This stagnation point sees direct contact with the fluid of the impinging jet.

Once the fluid has impinged on the surface, the fluid directs outward and creates a wall jet. This phenomenon is known as a hydraulic jump. A hydraulic phenomenon known as a hydraulic jump is widely seen in kitchen sinks, industrial applications, and manufacturing operations in addition to rivers and canals. The initial fluid speed has a significant role in the phenomena. No jump is possible if the fluid's starting speed is below the critical speed. A hydraulic jump happens at initial flow speeds that are higher than the critical speed. A circular hydraulic jump may occur some distance distant from the fluid jet impact site when it strikes a horizontal plate. Eventually, this hydraulic jump breaks free due to the combination of initial jet velocity and the surface roughness of the impinging surface. This hydraulic jump phenomenon can either be good or bad, depending on the engineering application.

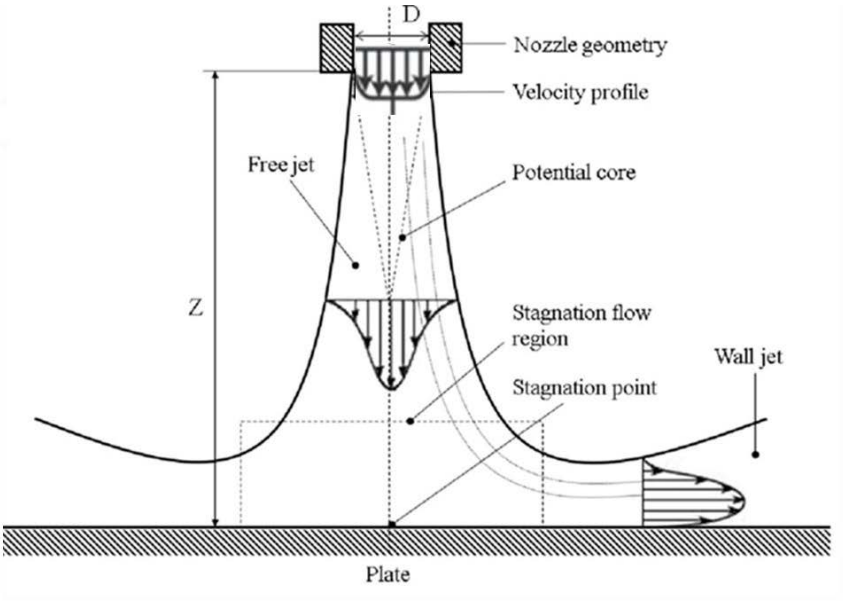

Figure 2.4: Free Surface Impinging Jet Schematic [67].

Heat transfer analysis of free surface impinging jets is reasonably simple to calculate. If the nozzle geometries are known, as well as the flow rate of the working fluid and the fluid properties, the Reynolds number can be calculated using Equation 2.7. For the heat transfer analysis, the use of the convection equation can be modified to accommodate the impinging jet temperature. Equation 2.19 shows the convection equation for an impinging jet apparatus. If the applied heat transfer rate is known, Equation 2.19 can be rearranged to solve for the HTC. Once the HTC is known, Equation 2.5 can be utilized to solve for the Nusselt number, which is a non-dimensional convection effect number.

$$\dot{Q}_{conv} = hA_s(T_s - T_{jet}) \tag{2.19}$$

To better understand free surface impinging jets, much research has been conducted. Friedrich et al. studied the effect of volumetric quality on heat transfer and fluid flow characteristics of two-phase free surface impinging jets [9]. The working fluids in his research consisted of air and water. Friedrich broke his results into three different regions of flow characteristics. Those are bubbly, slug, and annular regions. The bubbly region saw a linear increase in the Nusselt number as the volumetric quantity was increased. In the second region, slug flow, the Nusselt number increased exponentially until reaching its maximum point of volumetric quantity 0.8. The last region, annular flow, saw a decrease in heat transfer and fluid flow characteristics. Friedrich concluded that this decrease is related to the water jet column distortion with high air velocity.

Friedrich also studied the lateral variation of the Nusselt number and dimensionless hydraulic jump radius at two different Reynolds numbers. Results show that from the stagnation point to the hydraulic leap, the Nusselt number rapidly declines while the rate of heat transfer is high. Also, since a thin layer with a high flow velocity is present within the hydraulic jump due to a strong inertia force, a high heat transfer rate is achieved. Since gravity is a significant component in this area, the Nusselt number monotonically drops at the outside of the hydraulic jump.

Similarly, Choo also studied the heat transfer and fluid flow characteristics of two-phase free surface impinging jets [69]. The purpose of his research was to study the heat transfer characteristics of a two-phase impinging jet under a constant pumping power. Choo concluded that the convection effect increased as the volumetric fraction of the two-phase jet increased until a volumetric fraction between 0.2-0.3. Then, there was a present decrease in the Nusselt number due to water jet column distortion with high air velocity. Based on his experimental results, as a function of the volumetric percentage alone, correlations for the normalized stagnation and average Nusselt numbers of impinging jets were derived.

Liu and Lienhard studied the hydraulic jump in circular jet impingement [70]. During free surface jet impingement, they broke up the hydraulic jump phenomenon into four different categories. Those four categories are a jump without a roller, jump with a single roller, jump with a double roller, and an unstable jump with turbulent flow and air entrainment. To better depict the categories, Figure 2.5 shows schematics of the different hydraulic jumps. Liu and Lienhard concluded their work by adjusting the velocity nonuniformity of the separation by introducing a fictitious drag force. This equation is represented in Equation 2.20, while the Froude numbers for the subcritical and supercritical film are represented in Equation 2.21 and Equation 2.22.

$$2\pi\beta_\eta\left(\int_0^\eta \rho u(\beta_\eta, y)^2 dy - \int_0^\eta p\, dy\right) = -D2\pi\beta_\zeta\left(\int_0^\zeta \rho u(\beta_\zeta, y)^2 dy - \int_0^\zeta p\, dy\right) \quad (2.20)$$

$$F_{\beta_\eta} = \frac{ud^2}{g\beta_\eta\sqrt{g\eta^3}} \quad (2.21)$$

$$F_{\beta_\zeta} = \frac{ud^2}{g\beta_\zeta\sqrt{g\zeta^3}} \quad (2.22)$$

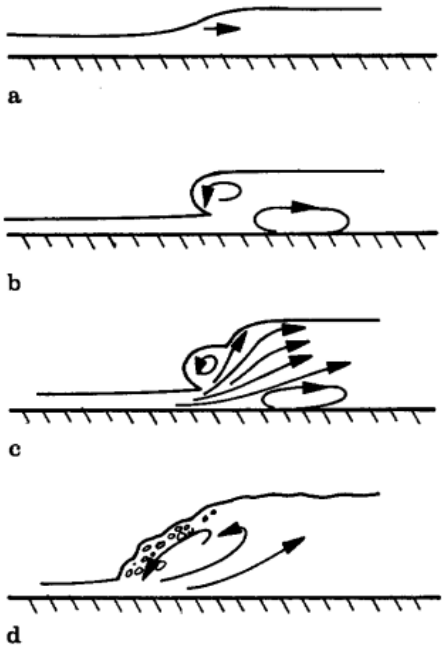

Figure 2.5: Hydraulic Jump Schematic (a) Jump Without Roller, (b) Jump With Single Roller, (c) Jump With Double Roller, (d) Unstable Jump With Turbulent Flow and Air Entrainment [70].

Similarly, Choo and Kim studied the influence of nozzle diameter on the circular hydraulic jump of liquid jet impingement [71]. The ongoing study aims to identify how the nozzle diameter affects the hydraulic jump radius for impinging jets operating at a fixed jet Reynolds number and impingement power. Choo and Kim utilized nozzle diameters ranging from 0.3-8 mm. Their results showed the hydraulic jump diameter increased with decreasing nozzle diameter under a constant flow rate. A novel correlation for the dimensionless hydraulic jump radius was put out as a function of the impingement power alone based on experimental findings. It was demonstrated that the dimensional analysis of the conservation equations had the same form as the hypothesized empirical correlation for the dimensionless hydraulic jump radius. Additionally, the outcomes unmistakably show that, as opposed to just one jet Reynolds number, the dimensionless hydraulic jump radius depends on both jet Reynolds and Froude numbers, two dimensionless groups.

Akansu studied an oblique slot impinging jet on a flat plate [68]. Akansu's goal was to determine the heat transfer characteristics on a flat and inclined plate using an obliquely slotted air impinging jet. Akansu concluded that the heat transfer characteristics on the horizontal plate are symmetrical and see a greater convection

effect with an increased flow rate. When the plate is subject to an angle, the highest heat transfer point changes from the geometric impingement point to the uphill side of the plate as the plate tilt rises. The heat transmission on the downhill side of the plate is greater than that on the uphill side at an inclination angle of 45° maximum.

Glaspell et al. studied heat transfer and hydrodynamics of air-assisted free water jet impingement at low nozzle-to-plate distances [72]. Glaspell's research was focused around low nozzle-to-plate distance (H/d = 0.02-0.51) air-assistant free water-impinging jets' heat transfer and fluid flow properties. The goal of Glaspell's research was to develop correlations based on experimental results for stagnation Nusselt number, hydraulic jump diameter, and pressure. During Glaspell's research, he found that the hydraulic jump diameter increased with decreasing nozzle-to-plate spacing under a fixed flow rate. He also concluded that the Nusselt number was proportional to the nozzle-to-plate spacing.

Kuraan also studied free surface impinging jets at low nozzle-to-plate spacings [73]. Kuraan used water as the working fluid. Similar to Glaspell, Kuraan's research was centered on water jet impingement with nozzle-to-plate spacing ranging from (H/d=0.08-1). Kuraan's research goal was to determine the free surface jet's stagnation pressure to better understand the effects of the Nusselt number and hydraulic jump diameter. The results of the experiment were divided into two regions, the jet deflection region and the inertia dominant region. In the jet deflection region, it was found that the Nusselt number and hydraulic jump diameter increase as the nozzle-to-plate spacing decreases. In the inertia dominant region, nozzle-to-plate spacing has little impact on normalized stagnation Nusselt number. Since the average jet velocity is constant, the jet deflection loss effect has vanished. This is indicated by the Nusselt number and hydraulic jump diameter.

Another important study on free surface impinging jets was conducted by Baonga. Baonga studied the hydrodynamic and heat transfer of free liquid jet impinging on a heated circular disk [74]. Baonga's focus in his research was to analyze the local and average thermal characteristics of the heat transfer coefficient on the heated disk. He did this by analyzing the film flow rate, the jet temperature, nozzle diameter, and nozzle-to-plate spacing. Baonga concluded on his work that the working nozzle describes most heat transfer characteristics. As the nozzle diameter increased, the Nusselt number increased on the impinging surface. Last remarks made by Baonga were breaking his results into three different zones. Those three zones are the impingement zone, the parallel flow zone, and the hydraulic jump zone. Each zone depends on the working Reynolds jet number.

2.3.2 Submerged Jet Impingement

Like free surface impinging jets, submerged impinging jets have the same features. The boundary conditions are the only difference between the free surface jet and the submerged jet. In order to make an impinging jet submerged, a wall boundary needs to be established. This wall boundary creates a fluid boundary around the impingning jet, hence a submerged impinging jet. The purpose of the submerged jet impingement is more fluid contact on the impinging surface. More fluid contact brings on more of a convection effect. To better understand how a submerged impinging jet works, Figure 2.6 shows a schematic of submerged jet impingement.

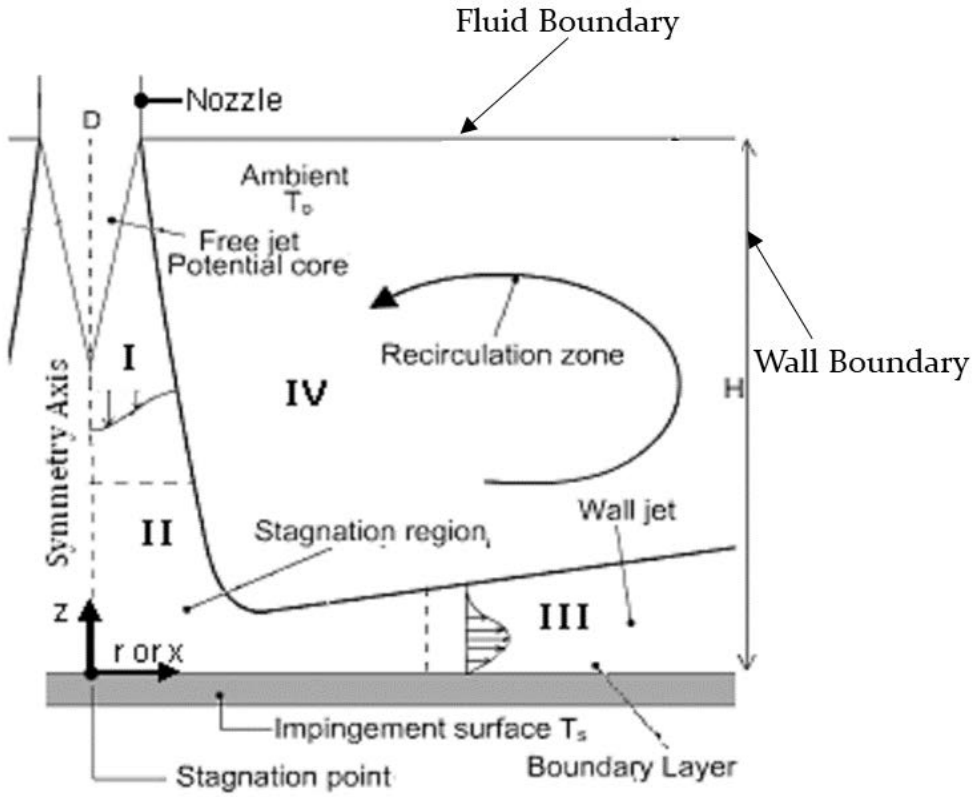

Figure 2.6: Submerged Impinging Jet Schematic [75].

Like a free surface jet, the submerged impinging jet schematic consists of D, the nozzle diameter, and Z or H, the nozzle-to-plate spacing. The fluid has reached its peak development for pipe flow at the nozzle's exit. The stagnation point is the exact center of the impinging plate. This point of stagnation comes into direct contact with the impinging jet's fluid.

Now is where the submerged impinging jet differs from the free surface jet. As stated previously, with the submerged impinging jet, there is now a present wall boundary that keeps the fluid in a control volume. This fluid now recirculates within the control volume until it overflows out of the wall boundary. The presence of this continuous fluid boundary allows for more fluid contact on the impinging surface. The submerged impinging jet also eliminates the effect of the hydraulic jump.

Heat transfer analysis of submerged impinging jets is calculated the same way as free surface impinging jets. By using the working flow rate and the nozzle geometry, the Reynolds number of the working fluid can be calculated. Similarly, the heat transfer rate can be calculated utilizing Equation 2.19. In order to produce a high heat transfer rate of submerged impinging jets, the temperature gradient needs to be larger when compared to the free surface jet. This larger temperature gradient is due to more fluid contact with the impinging surface due to the submerged impinging jet.

Just like free surface impinging jets, much research has been conducted on submerged impingning jets. Choo studied two-phase submerged impinging jets at different nozzle-to-plate spacings [76]. Choo studied H/d values ranging from H/d=0.1-40. The focus of Choo's research was to develop correlations for the normalized stagnation Nusselt number and pressure as a function of the nozzle-to-plate spacing. Choo broke his results into three different regions. Those regions are the jet deflection region, the potential core region, and the free jet region. Because the provided pumping power rises as the nozzle-to-plate separation decreases in region I, the normalized stagnation Nusselt number and dimensionless stagnation pressure dramatically increase. Since the average core velocity is constant in region II, the nozzle-to-plate separation has no impact on the normalized stagnation Nusselt number and pressure. Due to a decrease in jet velocity in region III, the normalized stagnation Nusselt number and pressure monotonically drop with increasing the nozzle-to-plate separation. Based on Choo's results, correlations were developed for the normalized stagnation Nusselt number and pressure. Those correlations are represented in Equation 2.23 and Equation 2.24. It is presented in both equations that the normalized stagnation Nusselt number and pressure are a function of the nozzle-to-plate spacing.

$$Nu^* = \sqrt{4e^{-\frac{\frac{H}{d}}{0.14}} + \left[0.57 - 0.5\tanh\left(\frac{\left(\frac{H}{d}\right)-15}{11}\right)\right]} \qquad 2.23$$

$$P^* = 4e^{-\frac{2\left(\frac{H}{d}\right)}{0.14}} + \left[0.57 - 0.5\tanh\left(\frac{2\left(\frac{H}{d}\right)-15}{11}\right)\right] \quad 2.24$$

Rouse studied two-phase free surface and submerged impinging jet. She used water and air as the working fluids [77]. Rouse's goal was to analyze both free surface and submerged impinging jet at different nozzle-to-plate spacings (H/d=0.03-8.5) and different volumetric quantities ranging from 0.1-0.9. Rouse concluded on her work by stating that the submerged jet had a higher Nusselt number at low nozzle-to-plate spacings when compared to the free surface jet. However, Rouse reported that the Nusselt number of the submerged jet fell linearly as the nozzle-to-plate distance grew, but the Nusselt number of the free surface jet rose linearly. Rouse finally concluded that the overall results, the submerged two-phase jet performed better than the free surface jet.

Li, Xuan, and Yu conducted research on submerged single-jet impingement using Cu water nanofluid [78]. These researchers sought out to combine both jet impingement and the use of a nanofluid for optimal heat transfer results. Li, Xuan, and Yu's research focus was centered around using Cu-water nanofluid with Cu particles of 25 nm and 100 nm. These nanofluid particles were then incorporated into a submerged impinging jet. On the heat transfer and flow performances of the nanofluids for the jet impingement, the impacts of the nanoparticle concentration, Reynolds number, nozzle-to-plate distance, fluid temperature, and nanoparticle diameter were discussed in their research. Upon completion of their research, they found that the performance of the base fluid's heat transmission is noticeably improved by the dispersed nanoparticles. Under the same Reynolds number, Cu-water nanofluid has a higher convective heat transfer coefficient than pure water. The volume percentage of Cu nanoparticles and the temperature of the nanofluid both affect how well heat transfers through the Cu-water nanofluid. Cu nanoparticles with a diameter of 25 nm in the nanofluid had a higher heat transfer coefficient than those with a diameter of 100 nm. A problem associated with using the Cu nanofluid when compared to pure water was the pressure drop. Li, Xuan, and Yu concluded that the pressure effects of the submerged impinging jet using nanofluids with different particle size had little to no effect when compared to pure water.

Chapter 3. Experimental Setup

The experimental work done for this research was completed with the implication of adding an impinging jet to a basic pool boiling setup. The goal was to take two different experimental procedures and combine them, which allowed an inclination toward empirical plausibility. Though not set up like the traditional pool boiling setup, missing the condenser and pressure transducer, accommodations needed to be made to introduce the impinging jet. Though the actions of the pool boiling phenomenon are the same, the experimental setup here was fabricated, assembled, and implemented solely for research purposes.

3.1 Wick Fabrication

While porous mediums utilize different materials such as ceramics and metals, the material used for this research consisted of copper metal. Copper is used in various heat transfer applications due to its high thermal conductivity and low specific heat, making its employment ideal for this investigation. A total of three different plates were utilized, a plain surface copper plate, a monolayer wick, and a columnar post wick. Each plate went through detailed fabrication to ensure proper functionality. The purpose of that functionality is to meet two critical parameters, reduce the Rayleigh-Taylor instability wavelength, λ_m through the capillary body for improved CHF, and reduce adequate wick thickness for the large HTC.

3.1.1 Plain Surface

The first plate utilized was the plain surface plate. The plain surface was fabricated using a commercially available, thin copper disk that measured 25 mm in diameter and had a thickness of 0.86 mm. The plain surface was cut to the size of the heater block's impinging surface to ensure constant heat flux. That size is 13 mm by 13 mm square copper plate. Measuring the instability wavelength for the plain surface, λp is the same as the critical Rayleigh-Taylor wavelength. Figure 3.1 shows a schematic of the behavior of the plain surface in pool boiling. Figure 3.2 shows a macroscopic image of the plain surface plate utilized for this research.

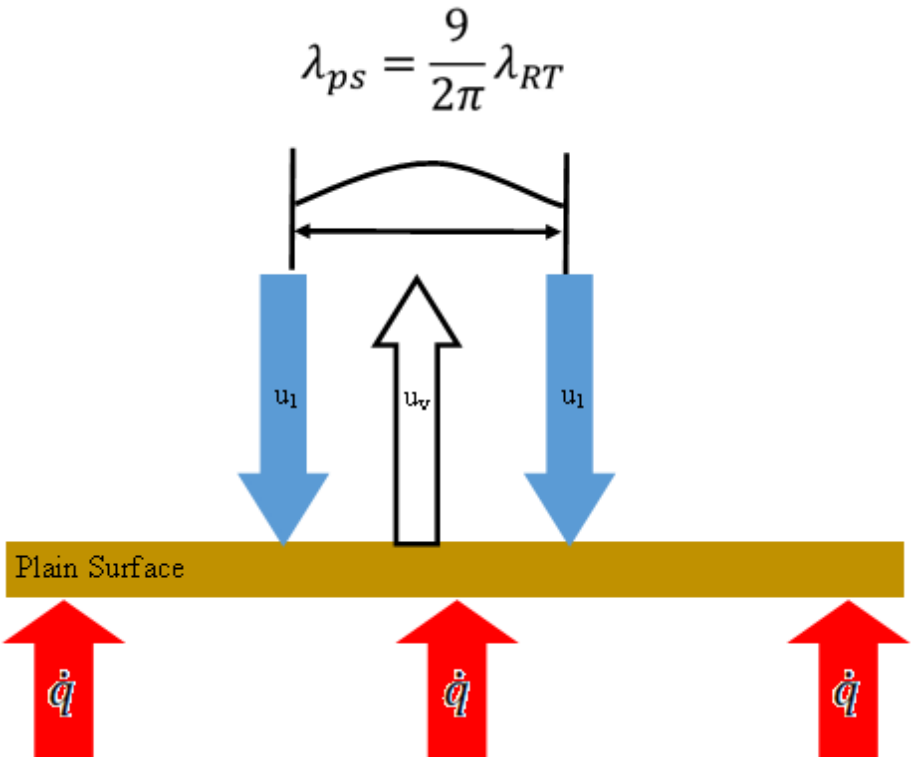

Figure 3.1: Pool Boiling Schematic of Plain Surface.

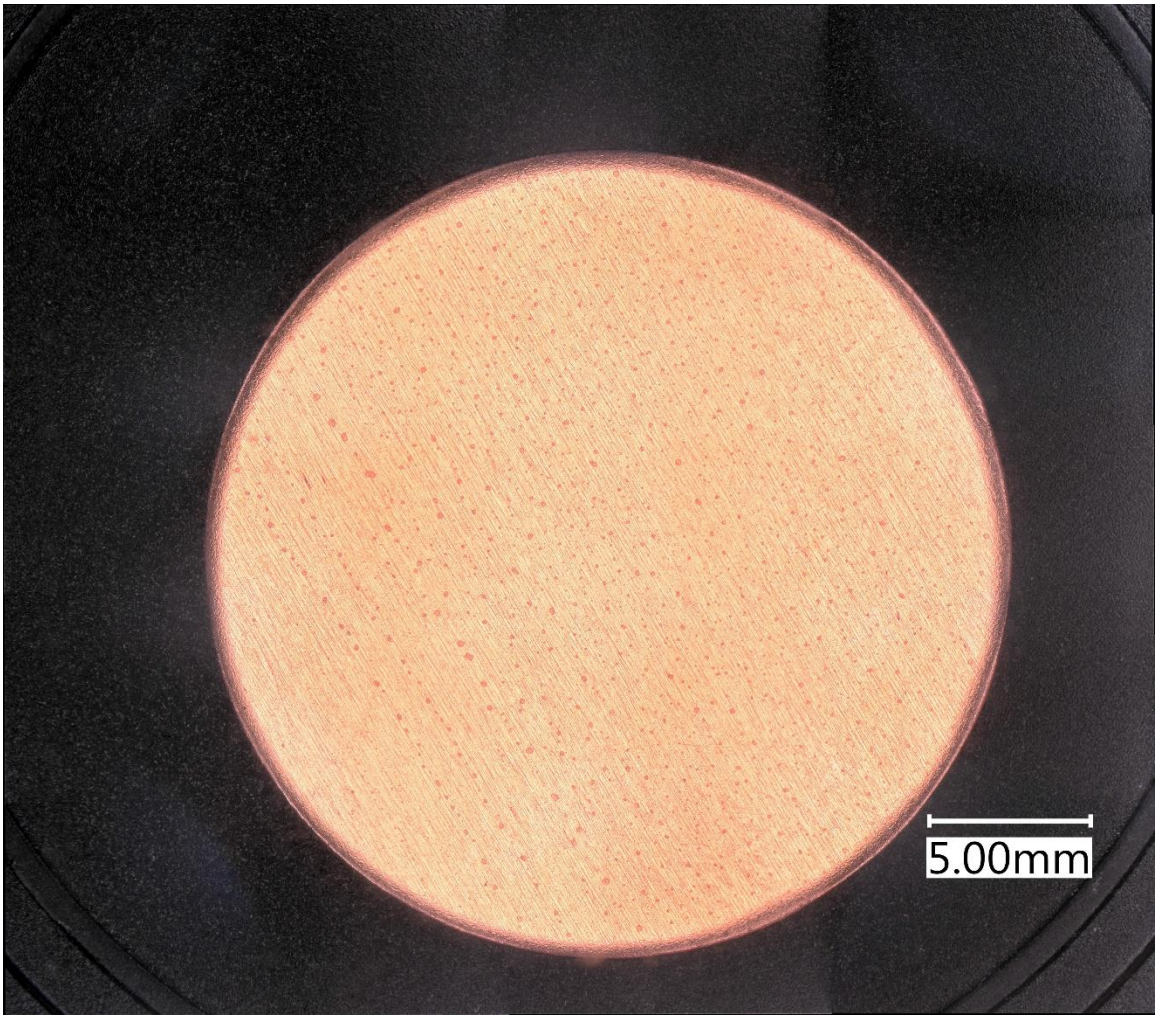

Figure 3.2: Macroscopic Image of Plain Surface Utilized for Experiment and Fabrication.

3.1.2 Monolayer Wick

Like the plain surface, the monolayer wick uses a commercially available copper disk as its base layer with the exact dimensions. In addition, introduced are copper-sintered particles with a diameter of roughly 200 μm. These copper-sintered particles make up the base layer of the monolayer wick. The purpose of the monolayer wick is to increase the HTC by decreasing the effective wick thickness. With the added monolayer surface comes a change in the instability wavelength. The instability wavelength is equal to the uniform wavelength. Figure 3.3 shows a schematic of the behavior of the monolayer wick in pool boiling.

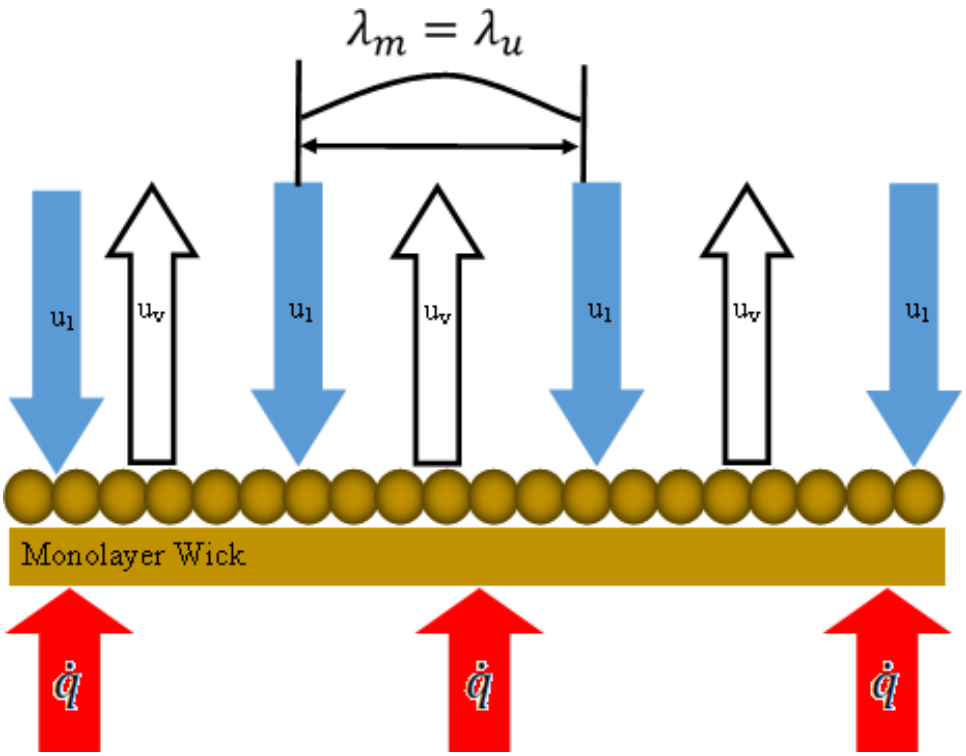

Figure 3.3: Pool Boiling Schematic of Monolayer Wick.

To fabricate the monolayer wick, a mold was filled with copper-sintered particles. Only one layer of copper-sintered particles was utilized, and careful consideration was used to ensure a uniform layer was applied. From there, the copper disk was applied to the top of the copper-sintered particles. The particle-covered plate was then placed into a furnace with 50 standard cubic centimeters per minute of argon gas. The furnace was set at 950°C, in which the monolayer wick sat for two hours. Upon completion of the two hours, the monolayer wick was removed and cooled via natural convection to ambient room temperature. The final monolayer wick was cut to 13 mm by 13 mm to ensure the constant heat flux boundary condition. Figure 3.4 shows the molding process for the monolayer wick. Figure 3.5 and Figure 3.6 show macroscopic and microscopic images of the monolayer wick.

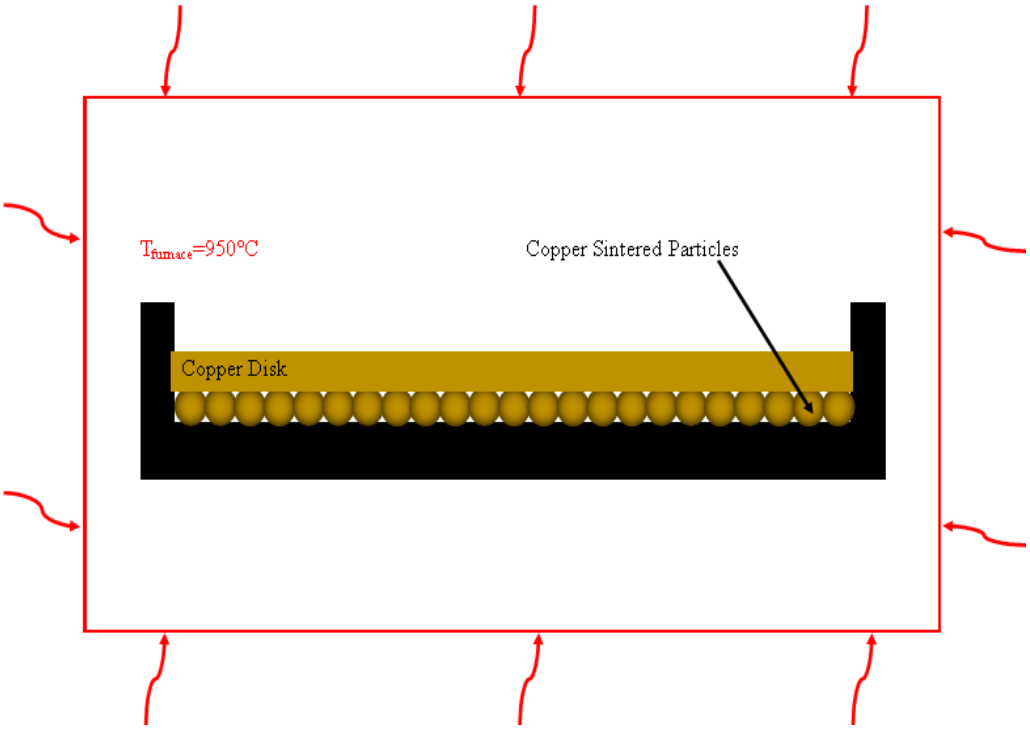

Figure 3.4: Molding Process for Monolayer Wick.

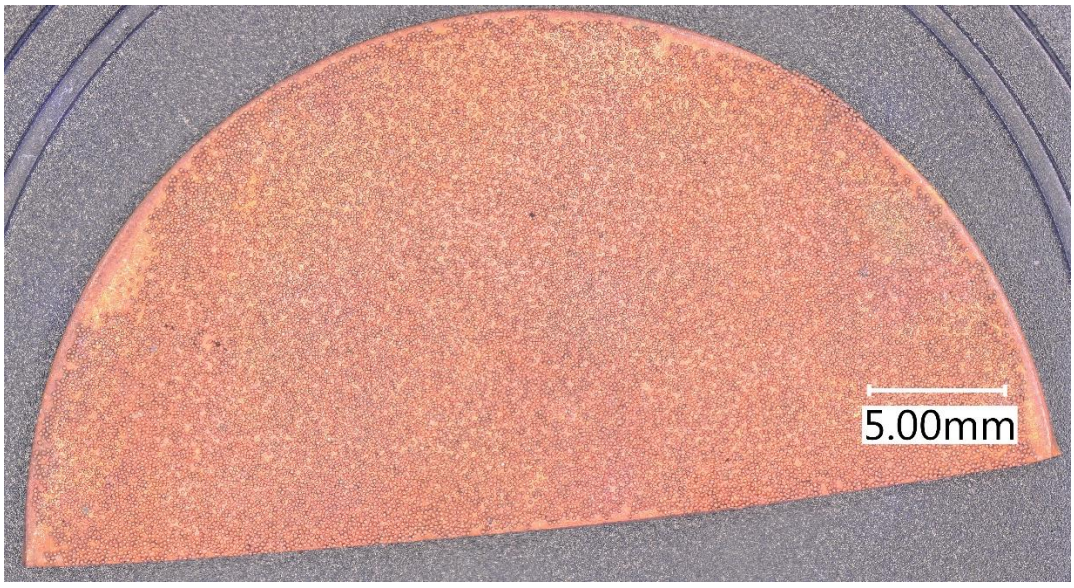

Figure 3.5: Macroscopic View of Monolayer Wick.

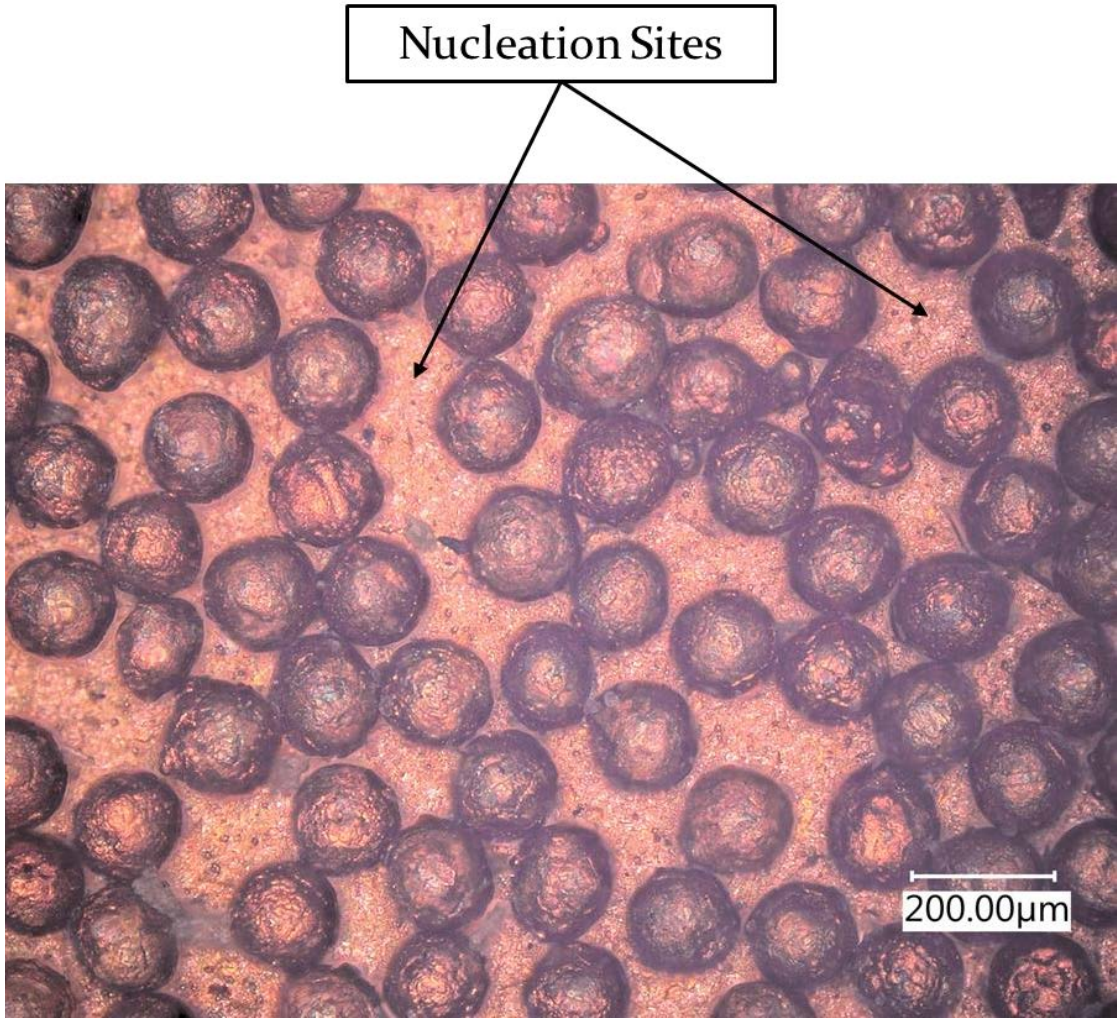

Figure 3.6: Monolayer Wick Particle Size.

3.1.3 Columnar Post Wick

Like the other two plates described previously, the columnar post wick uses the same commercially available copper disk with the exact dimensions. The same copper-sintered particles with a diameter of 200 µm were also employed. Like the monolayer wick, a base layer of copper-sintered particles was added to the columnar post structure. Utilizing those same copper-sintered particles, columnar posts were fabricated. Important details were paid close attention to in the design of the columnar post. Those essential details are the pitch distance, l_p, height of the columnar post, and the diameter of the columnar post. With the addition of the columnar posts, there is a present change in the instability wavelength. That instability wavelength now equals the pitch distance, which is 1 mm. Figure 3.7 shows a schematic of the behavior of the columnar post wick in pool boiling.

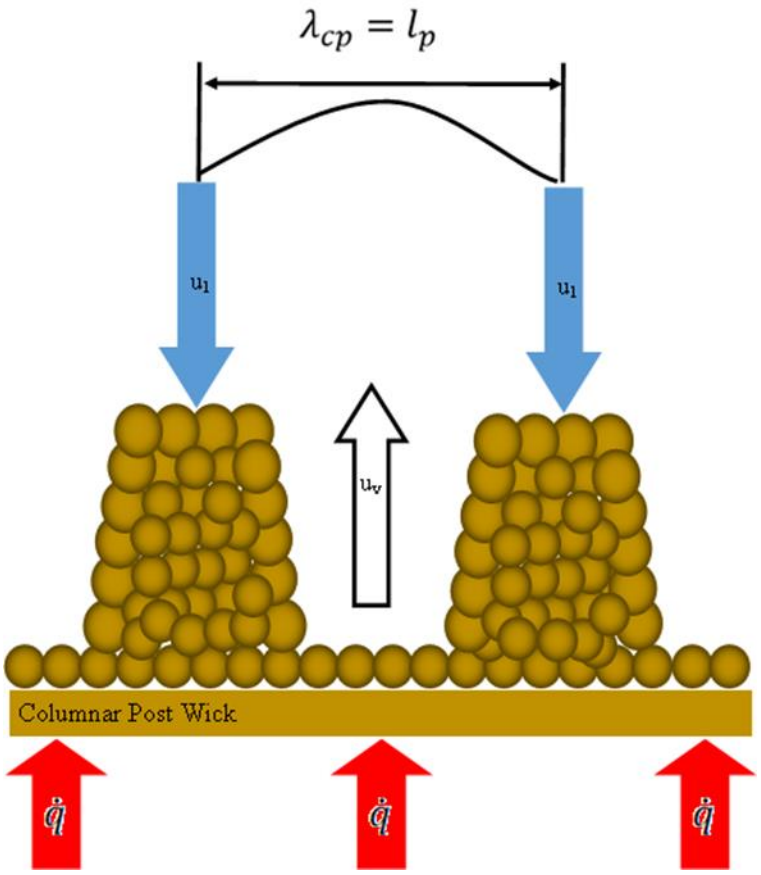

Figure 3.7: Pool Boiling Schematic of Columnar Post Wick.

To fabricate the columnar post wick, a different mold had to be used than that of the monolayer wick. Therefore, this mold was dwelled out to allow for the fabrication of the columnar post. The columnar post mold allowed for a pitch distance of l_p=1 mm, a post diameter of 2.5 mm, and a post height of 2 mm. The mold was filled with the 200µm copper sintered particles, filling the columnar post holes and allowing room for a single monolayer of particles. Placed atop the particles was a copper disk. Next, the columnar post wick was placed in the same argon furnace for two hours at 950°C. After two hours, the columnar post was cooled via natural convection to ambient temperature. The final columnar post wick was cut to 13 mm by 13 mm to ensure the constant heat flux boundary condition. Figure 3.8 shows the fabrication process of the columnar post wick. Figure 3.9 through Figure 3.11 show macroscopic and microscopic images of the columnar post wick.

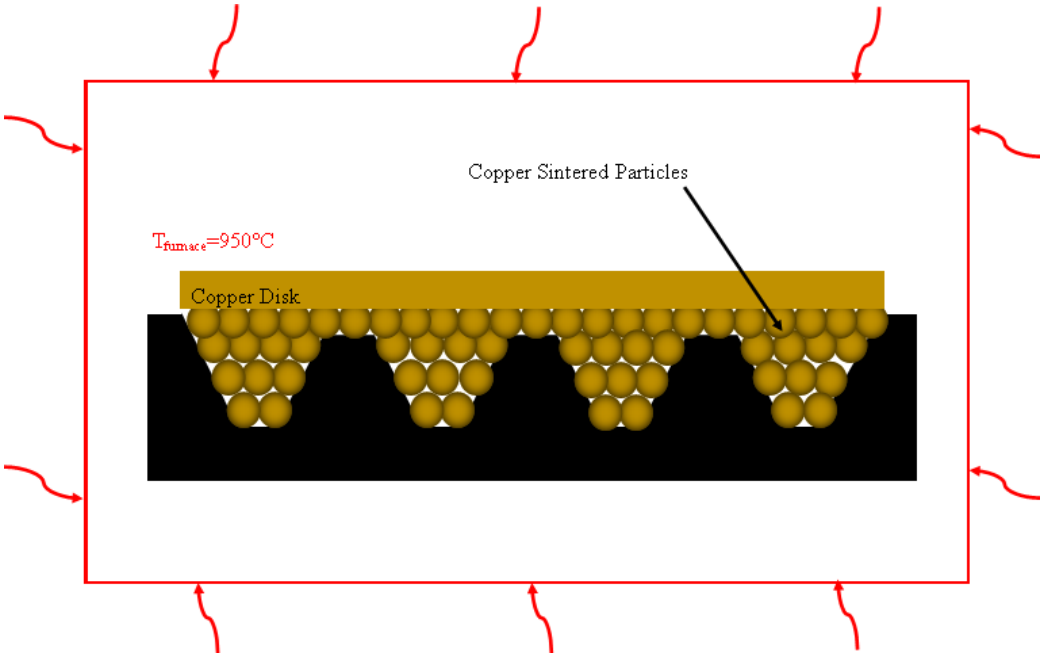

Figure 3.8: Molding Process for Monolayer Wick.

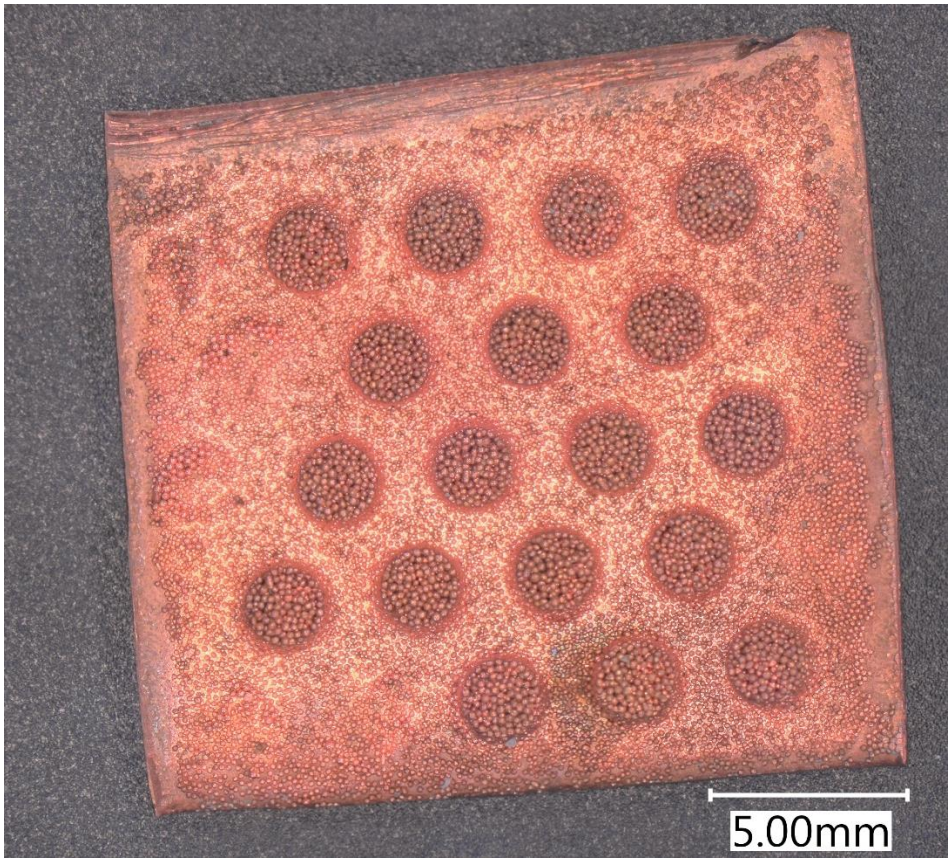

Figure 3.9: Macroscopic View of Columnar Post Wick.

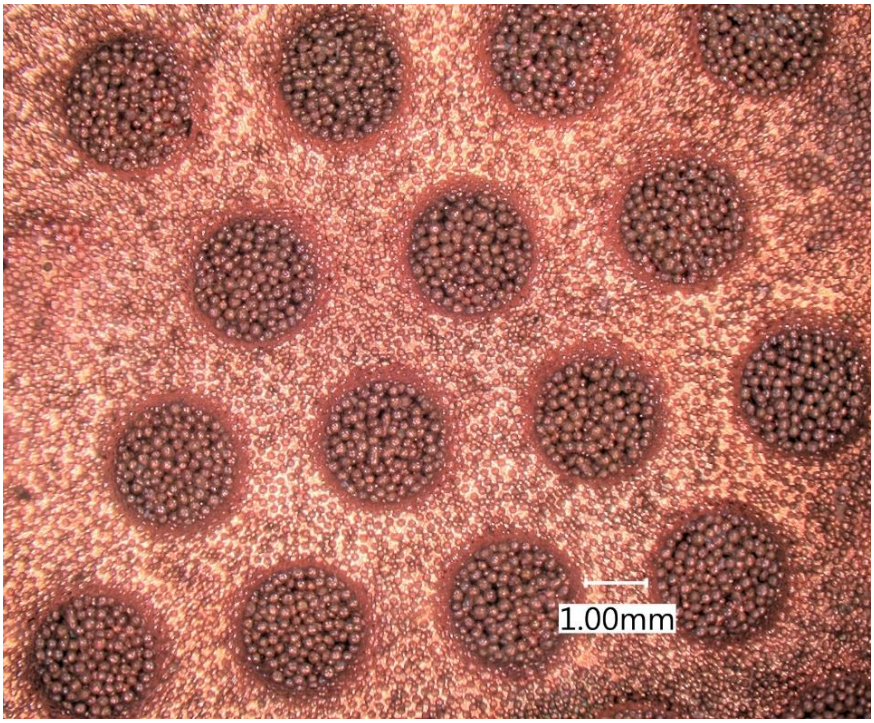

Figure 3.10: Pitch Distance of Columnar Post Wick.

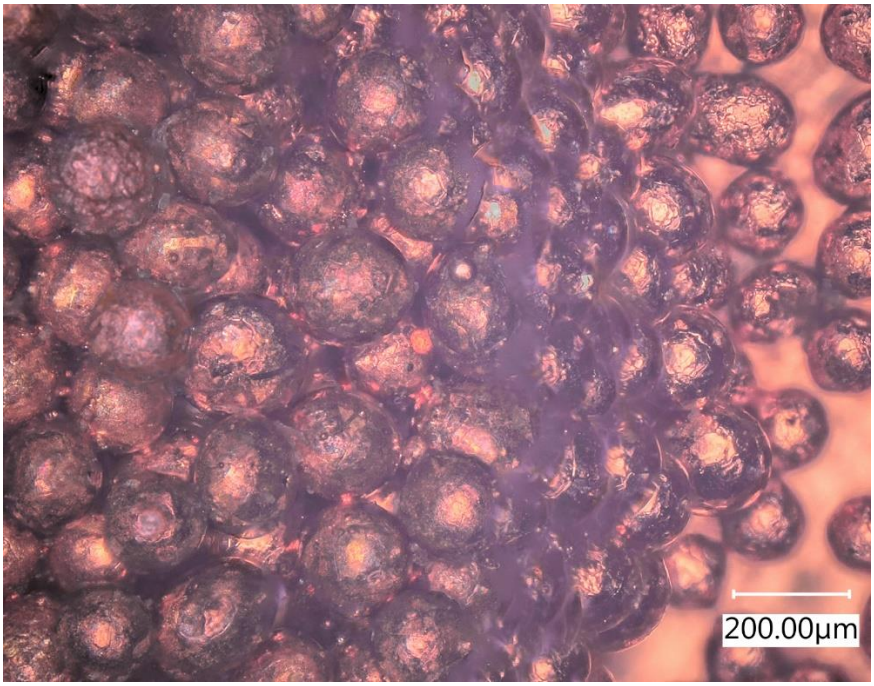

Figure 3.11:Columnar Post Wick Particle Size.

3.2 Heater Apparatus

The backbone of this research is the heater apparatus. The heater was designed around three main constraints. Those constraints are maintaining minimal heat loss, data collection feasibility, and fully modular capabilities. With those constraints considered, research was conducted into pool boiling setups. Like many pool boiling setups containing a pressure transducer, a condenser, and the boiling chamber, these components had to be removed to accommodate the impinging jet.

The design process started using a commercially available computer-aided design (CAD) software called SolidWorks. The material chosen for the heater was copper due to its high thermal conductivity rate of 398 W/m*K and low specific heat value of 0.39 J/g [82]. First, a copper base block was designed that allowed placement for six Tutco CH43810HW cartridge heaters. Atop the copper base block was another copper section that housed two K-type thermocouples that were spaced 20 mm apart from each other. These two K-type thermocouples will provide enough temperature data needed for proper calculations of results. Atop this copper section is the impinging surface, which housed the plain surface, monolayer wick, and columnar post wick. A solder joint was fabricated to ensure good contact between the top of the copper section and the plate/various wicks. The final copper housing was then machined for fabrication. Figure 3.12 shows the CAD drawing of the copper heater.

To ensure minimal heat loss, the copper heater had to be enclosed in an insulating material. The best material for this application is PTFE Teflon. PTFE Teflon has a very low thermal conductivity making it a good insulator. PTFE Teflon also has a high melting point making it an ideal material for this high-temperature application. The Teflon was machined into two parts, a top, and a bottom piece. The Teflon was cut out to allow cartridge heater wires, thermocouple wires, and the impinging surface. An insulation layer was used to fill in the gaps between the Teflon material and the copper heater. Figure 3.13 shows the different levels within the heater apparatus. Heavy-duty bolts were then used to fasten the heater apparatus together. Silicon was then placed in crevices to ensure a water-tight seal. Figure 3.14 shows the final assembly of the heater apparatus. For the submerged and pool boiling experiments, an acrylic tube was placed atop the impinging surface. To secure the acrylic tube and prevent leakage, silicon was placed on the bottom.

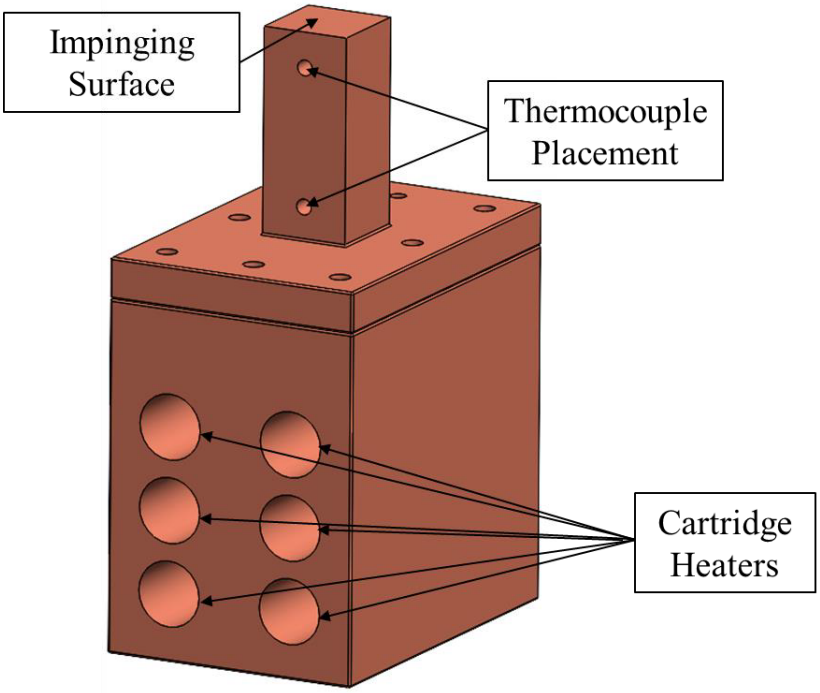

Figure 3.12: CAD drawing of Copper Heater Block.

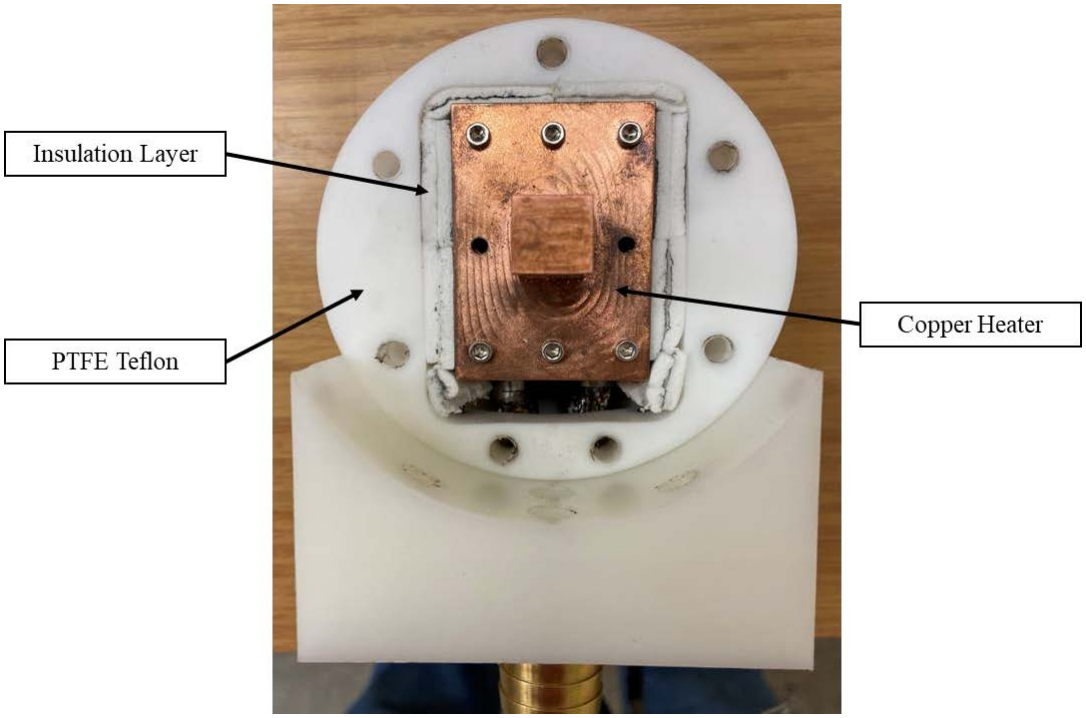

Figure 3.13: Inside of Heater Apparatus Showing Various Layers.

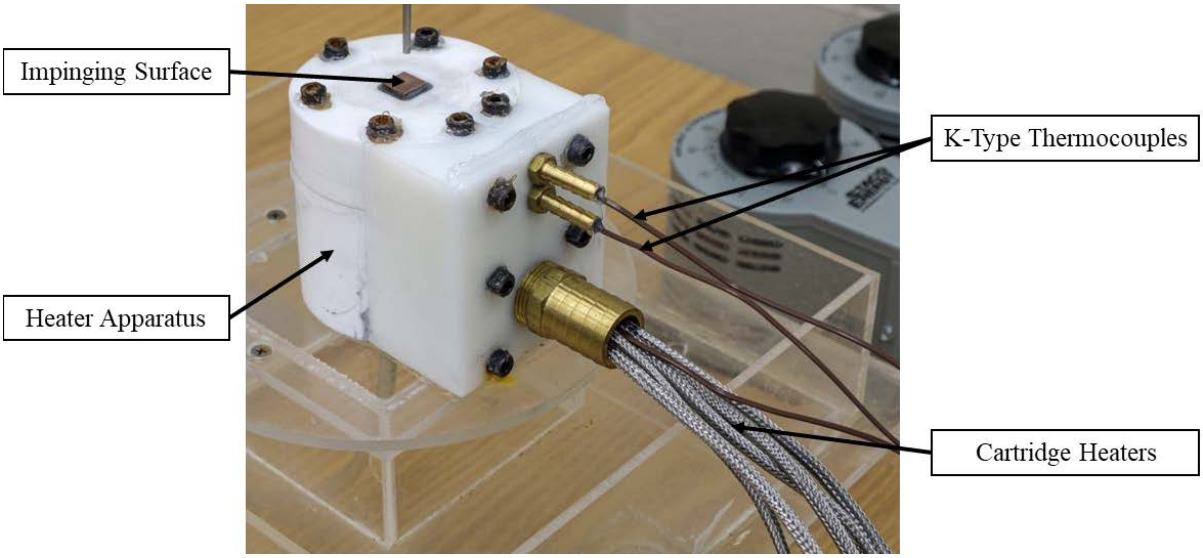

Figure 3.14: Fully Assembled Heater Apparatus.

Two variable transformers were used to control the amount of energy applied to the cartridge heaters. Staco Energy Products manufactured these variable transformers with model number 3PN10101B. These variable transformers have an input voltage of 120V and a variable output voltage of 0-140V. The current was kept constant at 10 Amps. Three cartridge heaters were connected in series to one variable transformer and were secured via wire nuts. Using these variable transformers allowed for ease of controlling the applied heat flux to the heater apparatus. Figure 3.15 shows the variable transformers used for this apparatus.

To record the temperature readings in real time, a temperature data recorder was used. The temperature data recorder used was an Omega OM-CP-QuadTemp2000. Thermocouples were plugged into the temperature data recorder, to which the temperature data recorder was plugged into a laptop. Two thermocouples were inserted into the heater apparatus as shown in Figure 3.12. Thermocouple number three was placed on the bottom of the heater apparatus to measure the temperature to ensure the heater was in a safe operating conditions. Lastly, the last thermocouple was used to measure the jet temperature. Figure 3.16 shows the Omega temperature data recorder.

Figure 3.15: Staco Energy Variable Transformers.

Figure 3.16: Omega Temperature Data Recorder.

3.3 Flow Apparatus

The flow apparatus was broken into two parts, a non-boiling flow apparatus, and a boiling flow apparatus. Starting with the non-boiling flow apparatus, a commercial water line was the primary source of the water supply. From there, flexible tubing was used to connect the commercial water line to a variable flow meter. The variable flow meter used for the non-boiling apparatus was a Dwyer RMB-82D-SSV with a flow range of 0-12GPH. Figure 3.17 shows the Dywer variable flow meter used for the non-boiling apparatus. From the variable flow meter, more flexible tubing was used to connect the variable flow meter to the nozzle. The nozzle used for both the non-boiling and boiling apparatus was an IDEX Health and Science stainless steel nozzle. The nozzle measured 100 mm in length, with an outer diameter of 1.60 mm, an inner diameter of 1 mm, and a thickness of 0.3 mm. The nozzle was mounted on a custom-built stand placed above the heater apparatus. The custom-built nozzle stand was equipped with two micrometers. These micrometers allowed for the movement of the nozzle in two directions. One direction is the height of the nozzle to the impinging surface, and the other is the movement of the lateral direction of the nozzle across the impinging surface. Figure 3.18 shows the nozzle and fabricated stand. Figure 3.19 shows a whole schematic of the non-boiling apparatus.

Figure 3.17: Dwyer Variable Flow Meter Used for Non-Boiling Experiment.

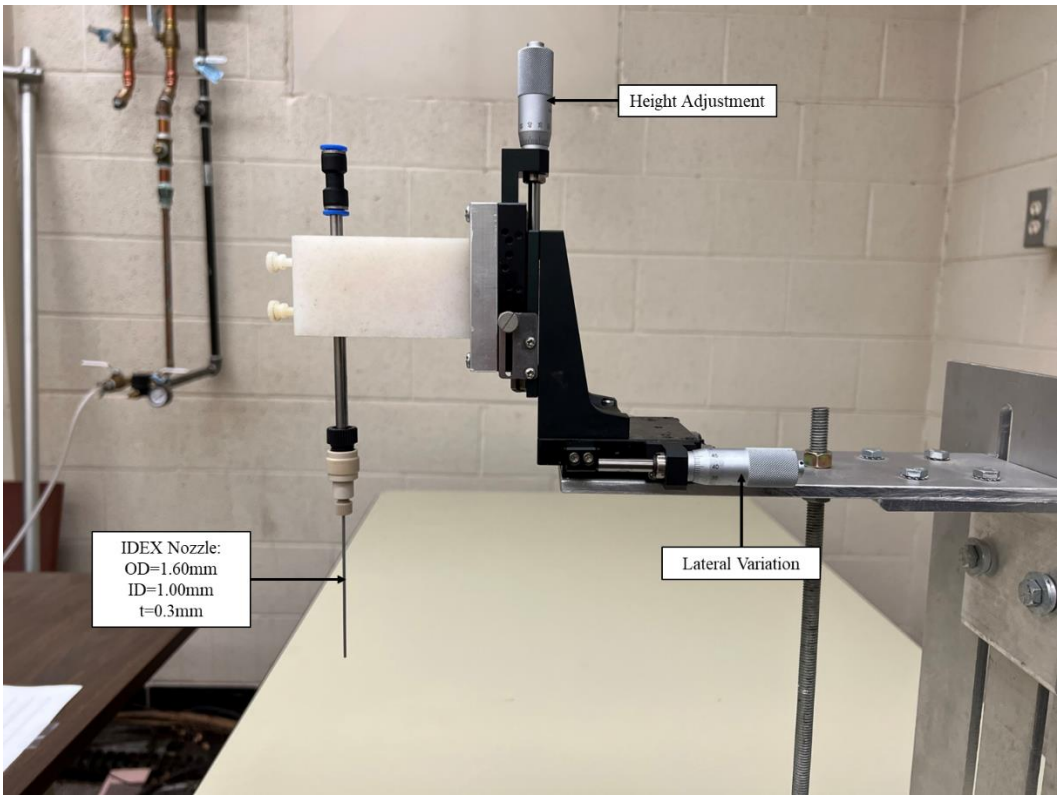

Figure 3.18: IDEX Nozzle and Fabricated Stand.

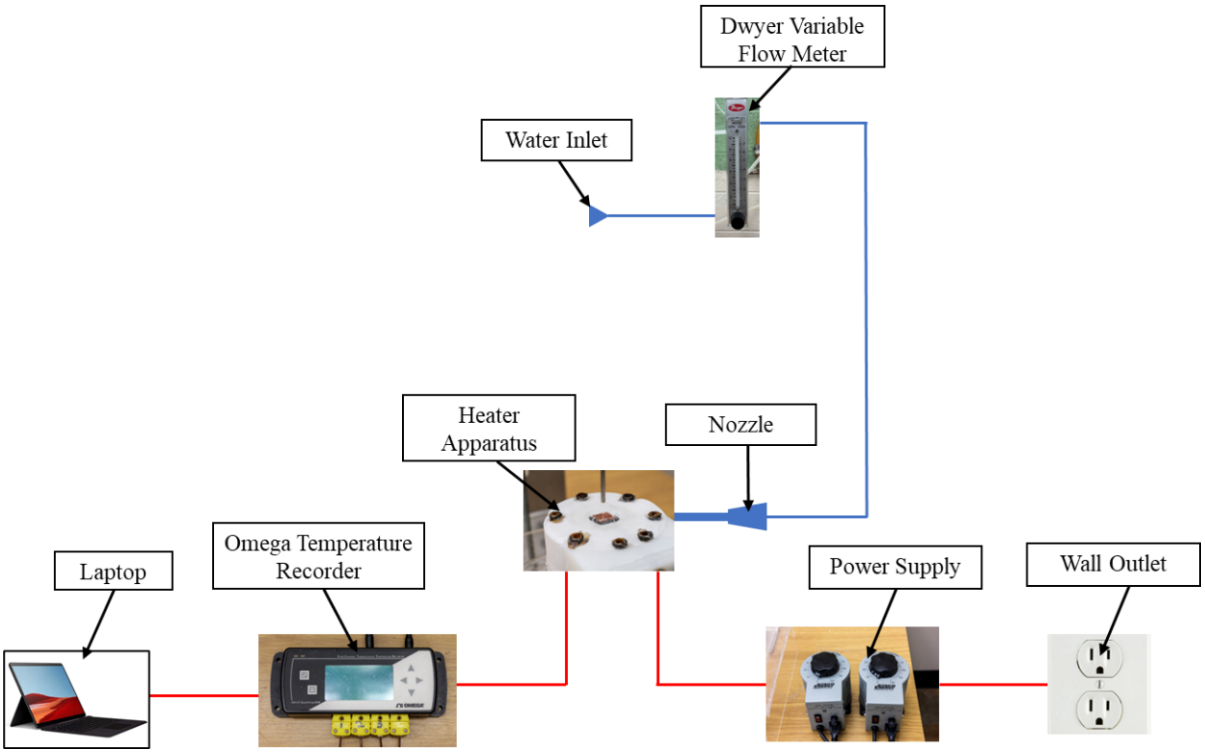

Figure 3.19: Schematic of Non-Boiling Experiment Apparatus.

For the boiling apparatus, instead of using the commercial water line, an Omega HCTB-3020 circulating hot temperature bath was used. This hot temperature bath was used to keep the temperature differential minimal between the impinging jet and the boiling surface. The Omega hot temperature bath had a temperature range of 40°C-120°C and maximum pumping power of 10 L/min providing the required needs for this research. Figure 3.20 shows the Omega hot water bath used. From the hot water bath, flexible tubing was used to connect another Dwyer variable flow meter. The Dwyer variable flow meter, model number RMA-33-SSV, had an operating range of 0-120 cc/min making it ideal for the low flow rate needed for the boiling apparatus. Figure 3.21 shows the Dwyer variable flow meter used for the boiling apparatus. From here, more flexible tubing connected the variable flow meter to the IDEX nozzle. All other components remain the same for the boiling flow apparatus. Figure 3.22 shows a schematic of the boiling apparatus.

Figure 3.20: Omega Circulating Hot Temperature Bath.

Figure 3.21: Dwyer Variable Flow Meter Used for Boiling Experiment.

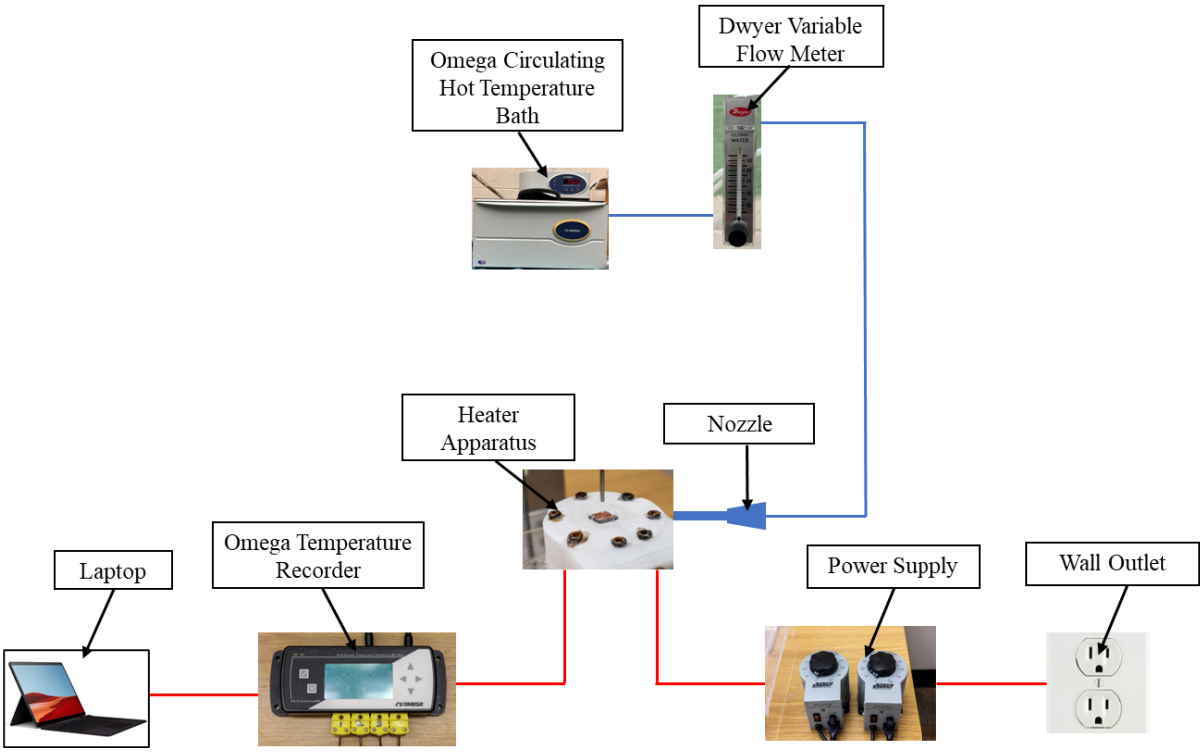

Figure 3.22: Schematic of Boiling Experiment Apparatus.

3.4 Procedure

3.4.1 Non-Boiling Procedure

Before the non-boiling experiment could begin, details such as flow rate, applied heat flux, and nozzle-to-plate spacing needed to be considered. The flow rate chosen for the non-boiling experiment consisted of flow rates ranging from 0.2-0.5 L/min. The reason for selecting these flow rates is to notice the hydraulic jump diameter increase. At 0.2 L/min was the first noticeable hydraulic jump. From there, it was settled that 0.5 L/min would be the final flow rate due to the high Reynolds number associated with that flow rate. The applied heat flux chosen for the non-boiling experiment was 100.17 W. This value was selected to provide enough heat flux without causing the surface to boil. Lastly, the nozzle-to-plate spacing, H/d, was set to seven. This value was chosen to allow adequate distance between the impinging surface and nozzle without causing harm to the different porous media. The impinging jet for the non-boiling experiment was set under two boundary conditions, a free surface jet and a submerged jet. To submerge the impinging jet, an acrylic tube was cut measuring 6.35 cm and adhered to the top of the heater apparatus using silicon.

First, the water supply was turned on, and the flow rate was set to the desired value. Then, with the water source applied, the two Staco Energy variable transformers were turned on and set to the desired applied heat flux. Before any data collection could happen, the steady state condition needed to be met. The steady-state condition was met when the temperature variation of the heater was ±0.5°C for a time interval of 10 minutes. Once the steady state condition was achieved, data collection happened in 10-minute intervals. To see the lateral variation change in Nusselt number, the nozzle was moved in 2 mm increments for a total of 6 mm distance in lateral variation. Figure 3.23 shows a schematic of the lateral variation change on the impinging surface. This process was repeated for each flow rate on the plain surface, monolayer wick, and columnar post wick under both free surface and submerged impinging jet boundary conditions.

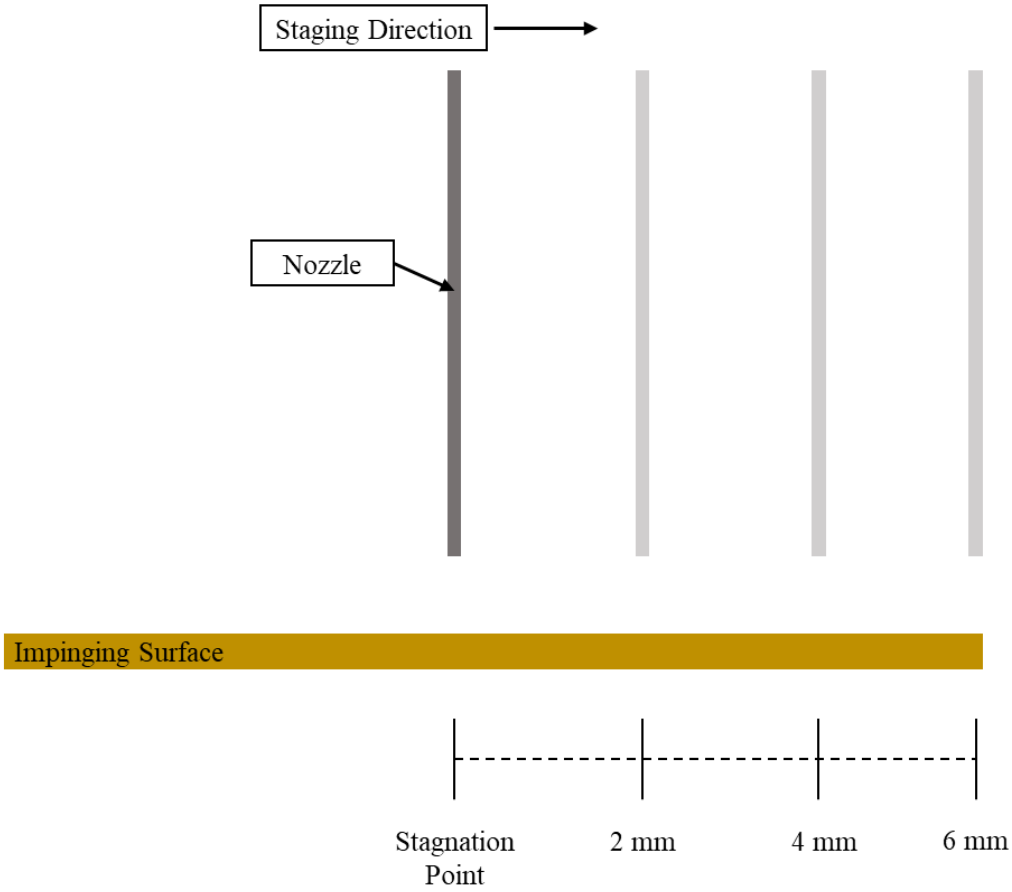

Figure 3.23: Schematic of Lateral Variation Change.

3.4.2 Boiling Procedure

As with the non-boiling procedure, a flow rate had to be chosen for the boiling procedure. The flow rates for the boiling procedure ranged from 0-0.08 L/min. These values were selected to allow for bubble generation in the boiling case without completely eliminating the boiling phenomena. The zero value notes that there was no impinging jet present for the experiment. Low flow rates were chosen such that during the boiling phenomenon; bubble generation was still present. Unlike the non-boiling procedure, which had constant heat flux, the boiling procedure had varying heat flux. The applied heat flux ranges differed depending on the surface/wick that was being utilized. The H/d was still set at seven to prohibit damage to the wick surfaces. The same 6.35 cm acrylic tube was utilized as a submerged surface needed to be present for boiling.

For the zero flow rate boiling experiment, the procedure is as follows. First, the acrylic cylinder was filled with water, and the two Staco Energy transformers were turned on. Plastic was then placed over the top of the acrylic cylinder to negate heat loss. From there, the applied heat flux was increased until bubble generation. Once bubble generation occurred, steady-state conditions had to be met until the temperature variation was ±0.5°C for a time interval of 10 minutes. Once steady state had occurred, data collection happened in 10-minute intervals. Next, critical heat flux was met when the temperature difference between the impinging surface and the saturation temperature was ~30°C or when surface dry-out was present. Once critical heat flux was obtained, the experiment was halted. This procedure was conducted for the plain surface and both wick surfaces.

For the boiling experiments with an impinging jet, the procedure is as follows. First, the Omega circulating hot temperature bath was turned on and set to 90°C. This was set below the boiling point to keep the temperature difference minimal between the nozzle and impinging surface. Once the circulating bath reached 90°C, the flow rate was set to the desired position, and the two Staco Energy variable transformers were turned on. Again, the applied heat flux was increased until bubble generation. The rest of the procedure follows the same as previously stated for both plain and wick surfaces.

Chapter 4. Results and Discussion

4.1 Non-Boiling Experiment

Two main results were sought for the non-boiling experiment. Those results are the relationship between the Nusselt number and Reynolds number and the lateral variation in the Nusselt number along the impinging surface. For validation purposes, the results were compared to literature reviews where appropriate. The non-boiling experiment was conducted under four different flow rates. Using those flow rates and the section properties of the nozzle, Reynolds numbers were calculated based on those flow rates. Table 4.1 summarizes the flow rates and calculated Reynolds numbers. Looking at Table 4.1, all those Reynolds numbers have a value greater than the 2,300 turbulent threshold for pipe flow, meaning the non-boiling experiment dealt strictly with turbulent flows. The plain surface and both monolayer wick and columnar post wick were analyzed with a goal in mind to determine the behavior under an impinging jet.

Table 4.1: Flow Rates for Non-Boiling Experiment with Corresponding Reynolds Number.

Flow Rate (L/min)	Reynolds Number
0.2	4234
0.3	6352
0.4	8469
0.5	10586

4.1.1 Free Surface Validation

To see if the validity of the experimental apparatus was adequate, an empirical correlation was used to compare the present study of this experiment. The empirical correlation used was that of researchers Webb and Ma [1]. Equation 4.1 shows the empirical correlation for free surface-impinging jets. This empirical correlation agrees to within 5% to 7% of other empirical correlations utilizing a Reynolds number range of 3,000 ≤ Re_w ≤ 40,000. In the turbulent Reynolds number range, Lienhard et al reports heat transfer coefficients for a fully developed pipe-type nozzle are 16% higher than the result of Equation 4.1 and nearly 60% higher than the laminar jet result [3]. This is most likely because the jets used to study splattering phenomena produce a lot of turbulence. Also, within the allowed percentage, falls in the nozzle to plate spacing of 1 ≤ H/d ≤ 10. It should be noted that Equation 4.1 forecasts stagnation heat transfer to be around 30% higher for typical jet impingement heat transfer than the laminar, uniform velocity jet of previous correlations, possibly because the pipe-type nozzle has an estimated 3–5% turbulence intensity. Figure 4.1 shows the empirical correlation plotted against the present study.

$$Nu_{stag} = 0.93 Re_w^{0.5} Pr^{0.4} \tag{4.1}$$

Here, the empirical correlation was plotted within ±10% of the mean value. The present study agrees with the empirical correlation to this ±10% with slight variation along the mean line. Also seen in Figure 4.1 are the calculated error bars for the present study. These error bars show the variability of the data and the uncertainty of the measurements. Equation 4.2 and Equation 4.3 show the error calculations. In Equation 2.3, “a” is the value of the data set, and “b” is the mean of the data set. “N” denotes the number of data points. All error bars had an uncertainty of less than 6%. Though not an exact match between the correlation and the present study, due to the turbulent flows, this correlation fits best. To measure the uncertainty in the heat flux and the Nusselt number, Equation 4.4 and Equation 4.5 was utilized which is the Kline and McClintock method.

$$SD = \sqrt{\frac{\Sigma |a-b|^2}{N}} \tag{4.2}$$

$$SE = \frac{SD}{\sqrt{N}} \tag{4.3}$$

$$U_q = q\left[\left(\frac{U_k}{k}\right)^2 + \left(\frac{U_{T1}}{\Delta T}\right)^2 + \left(\frac{U_{T2}}{\Delta T}\right)^2 + \left(\frac{U_{x1}}{\Delta x}\right)^2 + \left(\frac{U_{x2}}{\Delta x}\right)^2\right]^{0.5} \quad (4.4)$$

$$U_{Nu} = Nu\left[\left(\frac{U_k}{k}\right)^2 + \left(\frac{U_{kf}}{kf}\right)^2 + \left(\frac{U_q}{q}\right)^2 + \left(\frac{U_{T1}}{\Delta T}\right)^2 + \left(\frac{U_{T2}}{\Delta T}\right)^2 + \left(\frac{U_{x1}}{\Delta x}\right)^2 + \left(\frac{U_{x2}}{\Delta x}\right)^2\right]^{0.5} \quad (4.5)$$

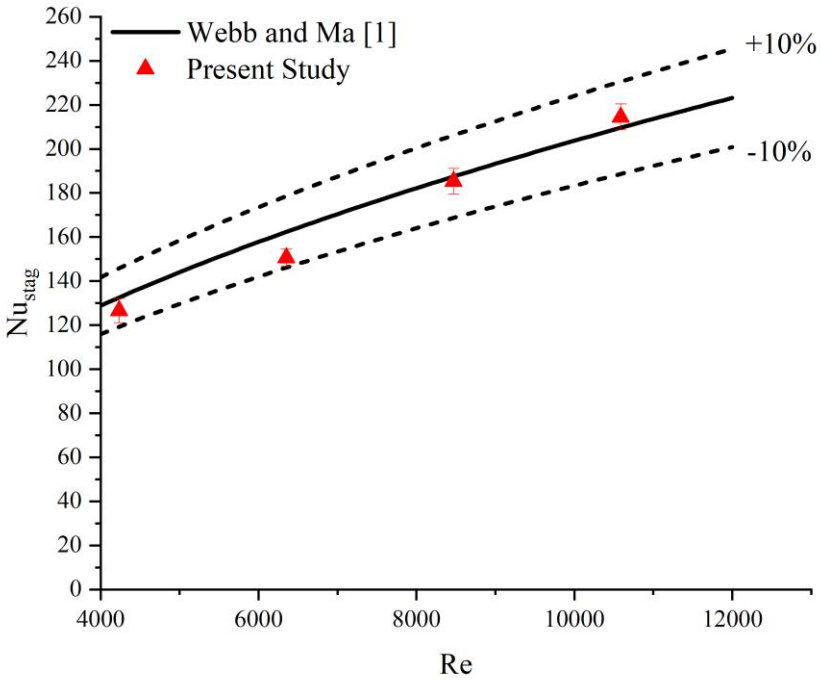

Figure 4.1: Non-Boiling Free Surface Validation Plot.

4.1.2 Free Surface Results

One apparent phenomenon with the free surface jet is the visible hydraulic jump. This hydraulic jump appears in fast-moving open flows when the flow becomes unstable. For this case, the chosen flow rates for this experiment all show a hydraulic jump. Figure 4.2 shows the flow rates and hydraulic jump increase on the different surfaces. It is apparent there is a sizeable hydraulic jump increase in both the plain surface and monolayer wick. This is due to both plates' flat surfaces, which makes the hydraulic jump phenomenon happen. This is not the case with the columnar post wick. Here, the post disrupts the free surface flow eliminating the causes for a hydraulic jump.

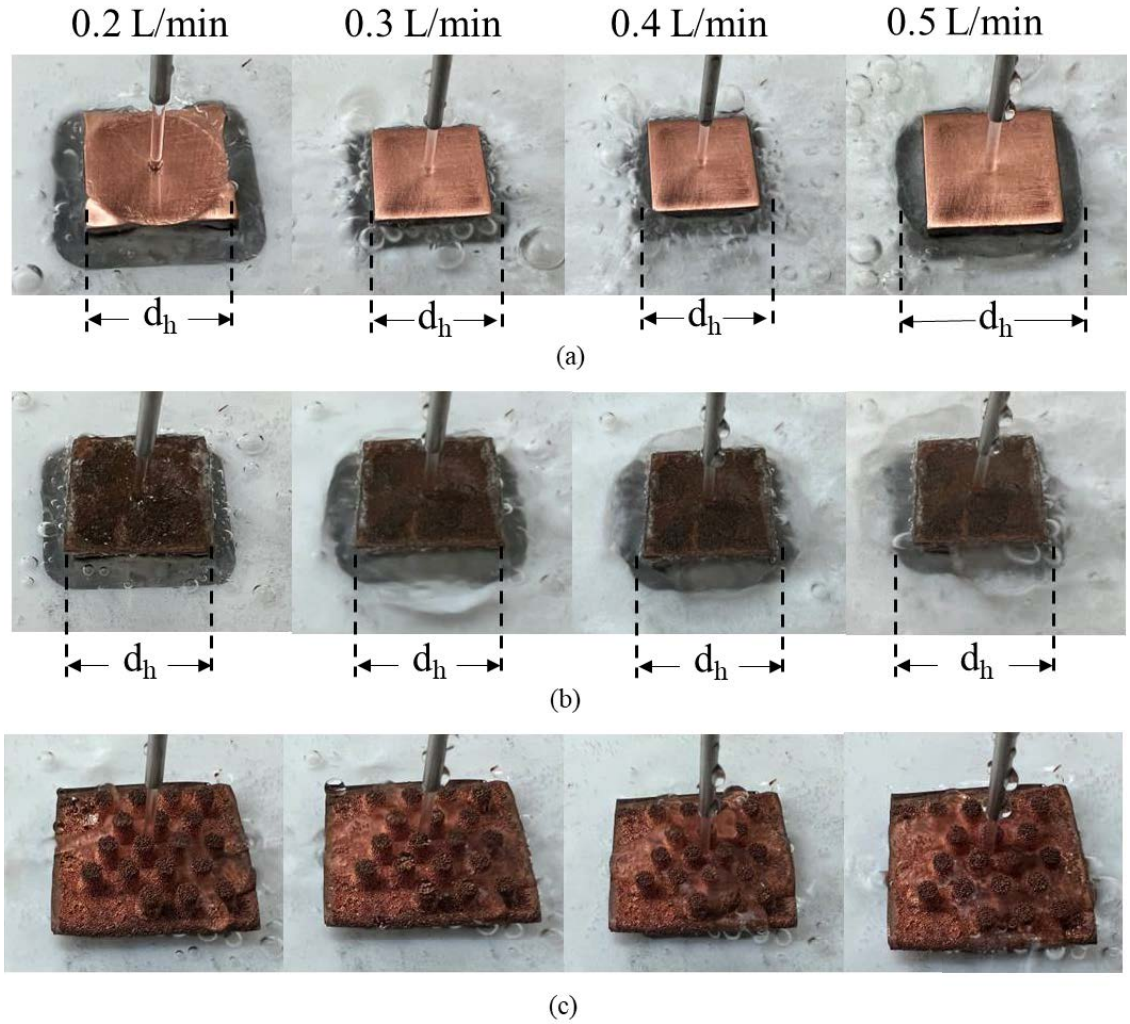

Figure 4.2: Hydraulic Jump Increase in Free Surface Case (a) Plain Surface (b) Monolayer Wick (c) Columnar Post Wick.

Next was to see the behavior of the plain surface, monolayer wick, and columnar post wick under a free surface impinging jet. First, the stagnation Nusselt numbers were plotted against the calculated Reynolds numbers for each flow rate. Figure 4.3 shows the stagnation Nusselt numbers versus Reynolds numbers. It is seen in Figure 4.3 that the plain surface outperforms both monolayer wick and columnar post wick. This is due to the polished surface of the plain copper plate. This polished surface allows for a uniform flow pattern on the impinging surface making the forced convection effect optimal for this surface. Though the monolayer wick also has a flat surface, the small copper-sintered particles create a rough surface over the plate. This rough surface slightly disrupts the flow pattern causing a decrease in the Nusselt number. The columnar post performs the least of the latter two. This is due to the columnar post and rough surface entirely disrupting the free surface flow.

Another reason for the decrease in the Nusselt number is the greater conduction effect of both monolayer wick and columnar post wick. Though previous research of the monolayer wick shows an increase in HTC due to the increased effective thermal conductivity, the impinging jet did not produce a significant enough convection effect to overpower the conduction effect [5]. The same is to say for the columnar post wick. The thick porous layer of the columnar post wick increases the conduction path, which produces a more significant conduction effect. This results in a lower Nusselt number when compared to the plain surface. This convection effect overruled the conduction effect, resulting in a higher Nusselt number.

The behavior of the relationship between the Nusselt number and the Reynolds number is linear for all three plates. The slope of the lines is greatest with the plain surface with a decreasing gradient from the monolayer wick to the columnar post wick. The high rate of change of Nusselt number for the plain surface is again due to the polished surface of the plain surface. The same is to say for the monolayer wick and columnar post wick. The slope is less with these two due to the surface roughness of the monolayer wick and the post structures of the columnar post wick. These factors play a role in the decrease in the rate of change between the Nusselt number and the Reynolds number.

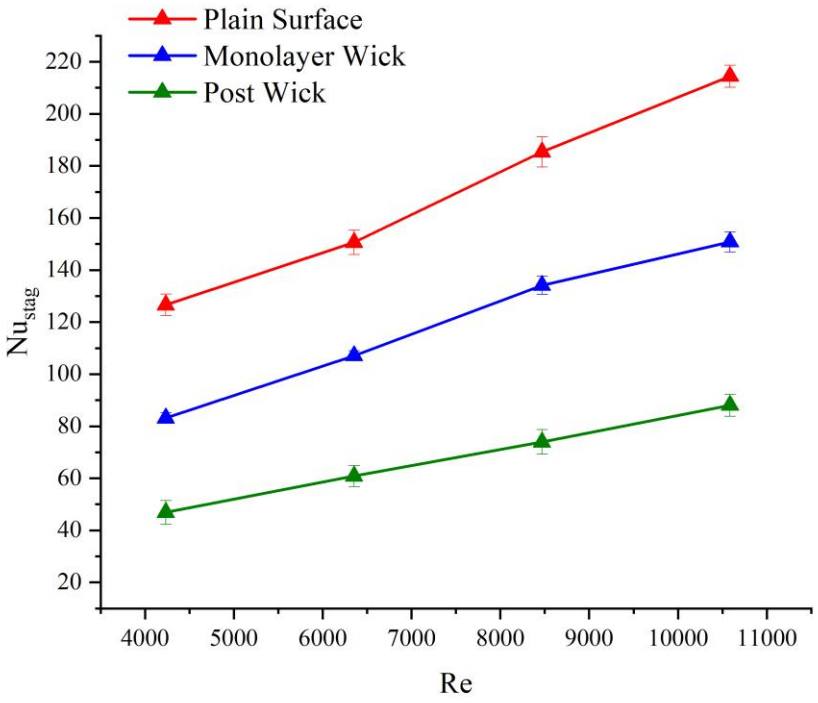

Figure 4.3: Stagnation Nusselt Number vs. Reynolds Number for Free Surface Case.

The next result investigated was the variation in the Nusselt number as the nozzle moved away from the stagnation point. This experiment was again analyzed at the four different Reynolds numbers, as seen in Table 4.1. The nozzle was moved away from the stagnation point in 2 mm increments for a total of four different positions. The lateral distance, r, was then divided by the nozzle diameter, d, to keep items non-dimensional. Figure 4.4 through Figure 4.7 show the Nusselt number variation along with the nozzle position lateral change for each flow rate.

It is present in the plots that there is a change in the Nusselt number as the nozzle moves away from the stagnation point. The most significant change is with a Reynolds number of 4,234. This has the greatest change in the Nusselt number due to this Reynolds number producing the smallest hydraulic jump. Increasing the flow rate decreases the variation in the Nusselt number. Looking at each specific plate, the plain surface shows the greatest change, while the columnar post shows little to no difference, especially at a higher flow rate. This stems back to the topology of each individual plate. The plain surface allows for uniformity in impingement during lateral variation showing a present decrease away from the stagnation point. This is not the case with the columnar post wick. During lateral nozzle variation, the impinging fluid is disrupted by the columnar post, resulting in a constant Nusselt number. Also, the columnar post allows for even heat dissipation. This even heat dissipation forms a uniform temperature distribution resulting in the slight change in the Nusselt number along the columnar post wick.

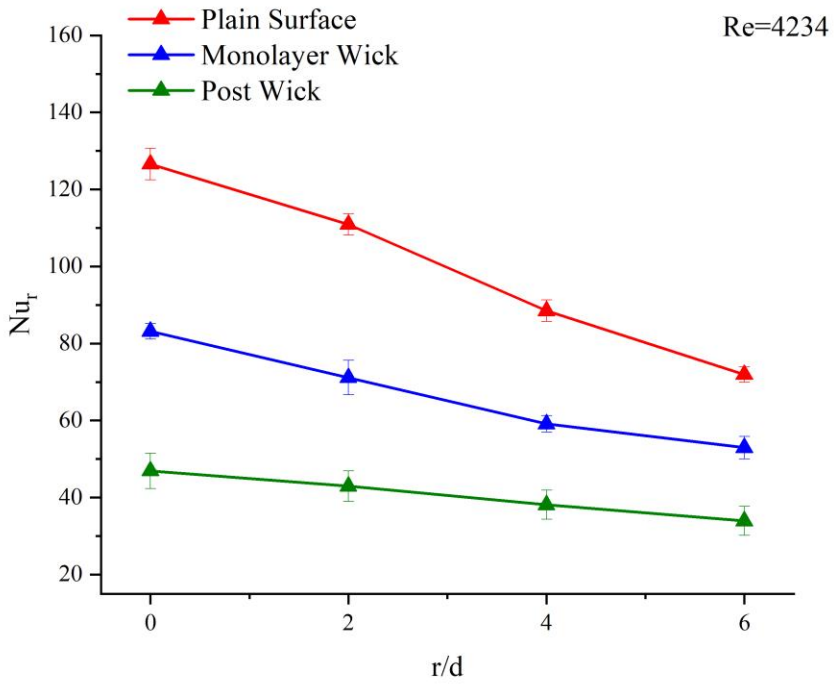

Figure 4.4: Nusselt Number vs. Lateral Variation for Re=4234 (Free Surface).

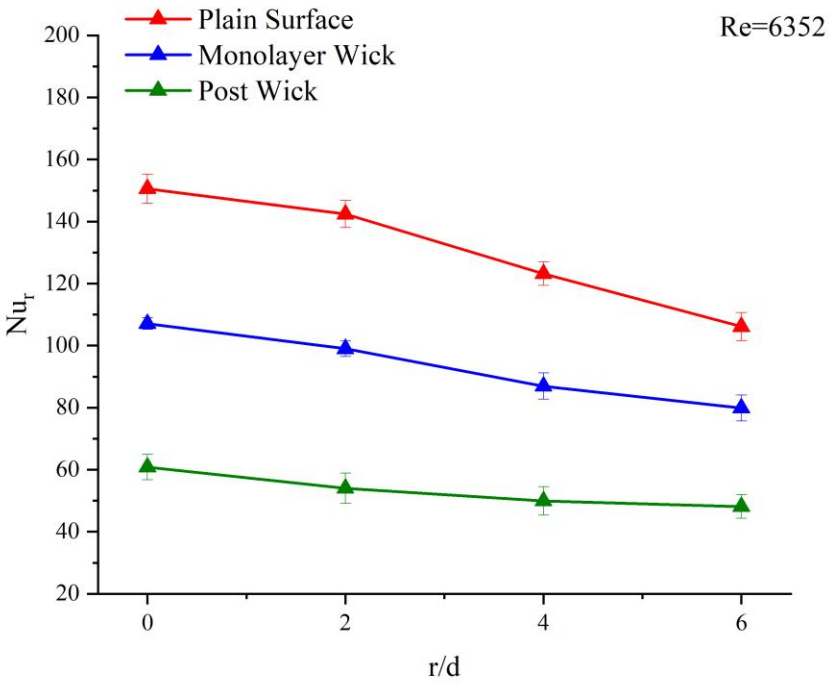

Figure 4.5: Nusselt Number vs. Lateral Variation for Re=6362 (Free Surface).

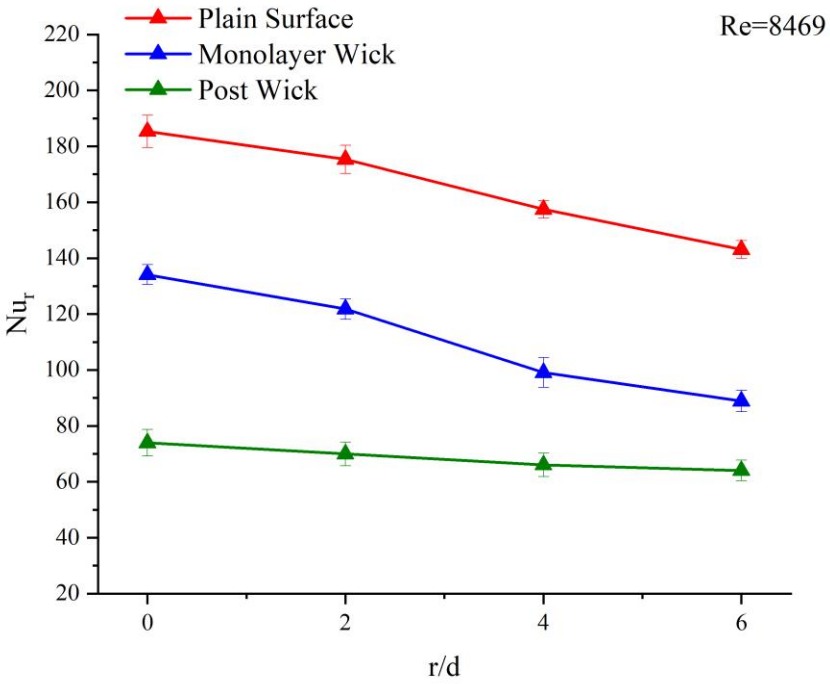

Figure 4.6: Nusselt Number vs. Lateral Variation for Re=8469 (Free Surface).

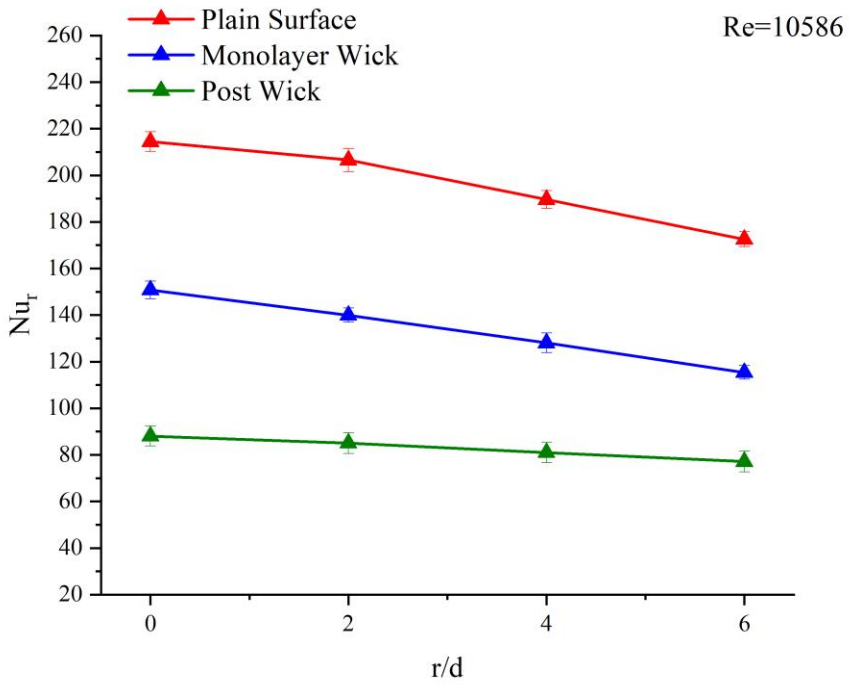

Figure 4.7: Nusselt Number vs. Lateral Variation for Re=10586 (Free Surface).

4.1.3 Submerged Results

With the free surface case, there was a hydraulic jump present. However, this phenomenon does not occur with the submerged case. Upon submerging the impinging jet, the whole impinging surface also becomes submerged. This allows the impinging surface complete fluid contact and eliminates the hydraulic jump. Figure 4.8 shows the behavior of the different plates under a submerged impinging jet. Looking at Figure 4.8, each plate has complete fluid contact, and no hydraulic jump is present.

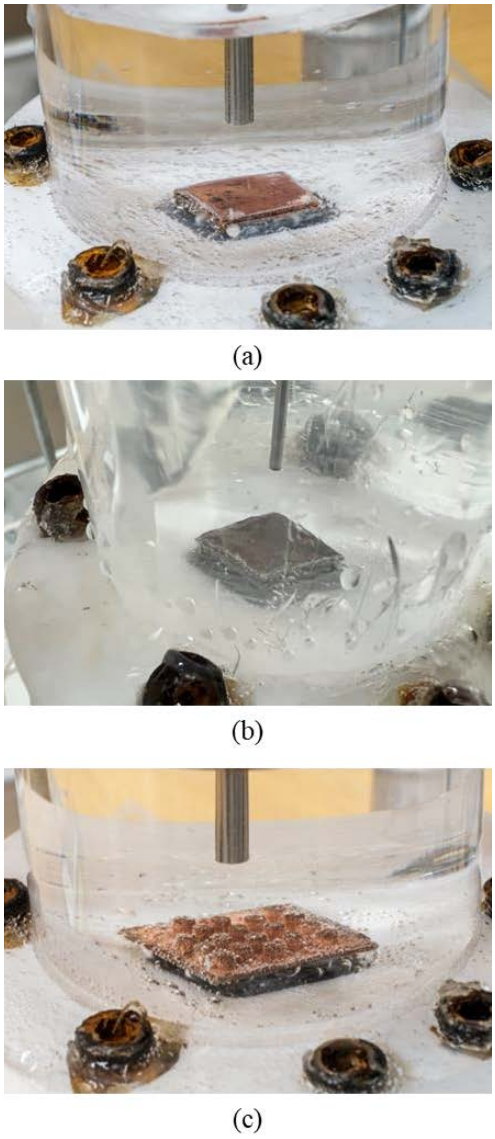

Figure 4.8: Submerged Impinging Jet on all Plate Types (a) Plain Surface (b) Monolayer Wick (c) Columnar Post Wick.

Next was to see the behavior of the plain surface, monolayer wick, and columnar post wick under a submerged impinging jet. Again, the stagnation Nusselt numbers were plotted against the calculated Reynolds numbers for each flow rate. Figure 4.9 shows the stagnation Nusselt numbers versus Reynolds numbers under a submerged impinging jet. It is present again that the plain surface outperforms both monolayer wick and columnar post wick. This is again due to the polished surface of the plain surface, while the latter two plates have rough/heightened surfaces. Also, the convection effect of the impinging jet is greatest with the plain surface. Both monolayer wick and columnar post wick have greater conduction effects resulting in a decreased Nusselt number. Comparing the Nusselt numbers of the submerged impinging jet to the free surface impinging jet, all Nusselt numbers are higher in the submerged impinging jet case. This is due to the submerged impinging jet having complete fluid contact with the impinging surface. For example, the columnar post wick, in the free surface case, was exposed to air atop the post.

The behavior of the relationship between the Nusselt number and Reynolds number is again linear for all three plates. However, there is a present anomaly with the columnar post wick. This error could come from the impinging jet hitting one of the posts during the experiment causing the change in trend. Another factor could be a fluid contact disturbance along the post. The slopes of all three surfaces behave in a similar manner. This slope change is due to the submerged boundary condition, which is different from the free surface case.

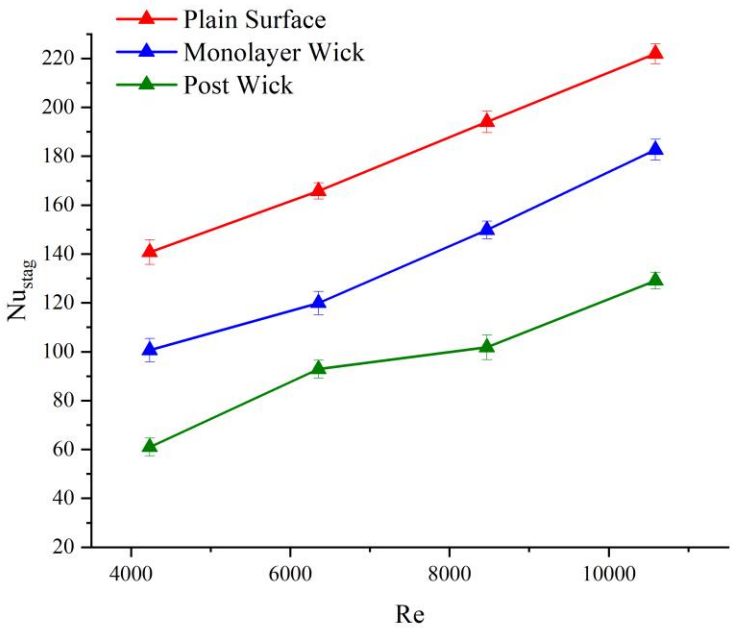

Figure 4.9: Stagnation Nusselt Number vs. Reynolds Number for Submerged Case.

The following result looked at was the variation in the Nusselt number as the nozzle moved away from the stagnation point for the submerged case. Utilizing the same four Reynolds numbers as seen in Table 4.1, the experiment was conducted. This experiment was done to compare the free surface case to the submerged case. The goal was to determine if there is less change in the Nusselt number during lateral variation. Figure 4.10 through Figure 4.13 show the Nusselt number variation along with the nozzle position lateral change for each flow rate.

It is present in the Figures below that there is again a change in the Nusselt number as the nozzle moves away from the stagnation point. The most significant change occurred in the plain surface plate for all Reynolds numbers investigated. Even though no hydraulic jump is present, there is a present change in the Nusselt number due to the small nozzle diameter that was used for the experiment. Each flow rate shows a significant decrease in the Nusselt number, especially the plain surface and monolayer wick. The columnar post wick shows the least decrease in Nusselt number due to the post disrupting the flow field.

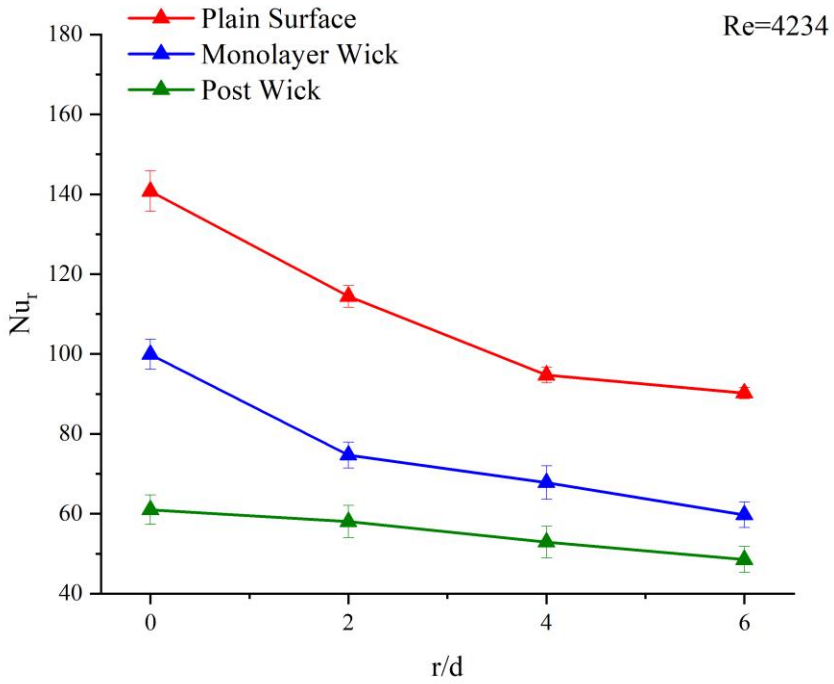

Figure 4.10: Nusselt Number vs. Lateral Variation for Re=4234 (Submerged).

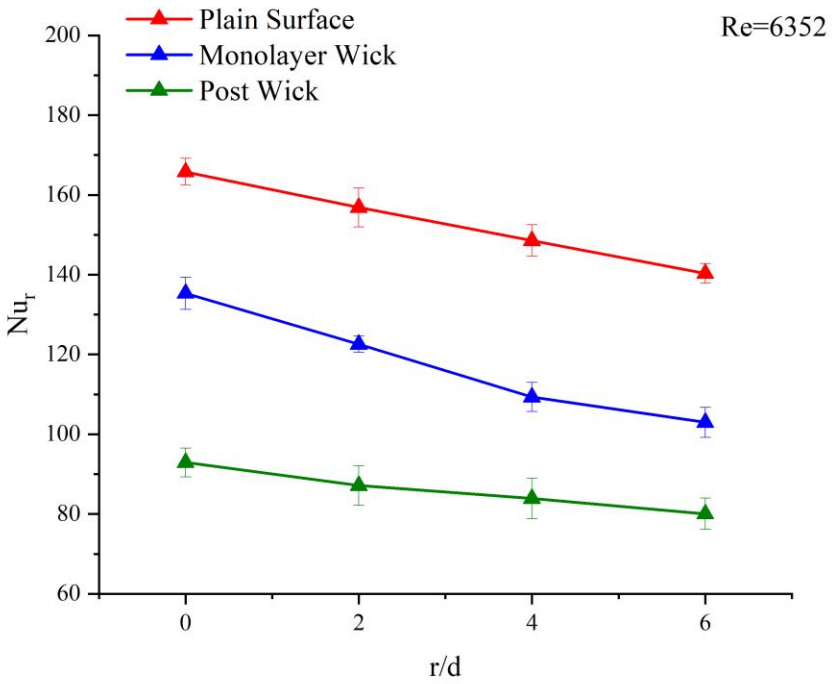

Figure 4.11: Nusselt Number vs. Lateral Variation for Re=6352 (Submerged).

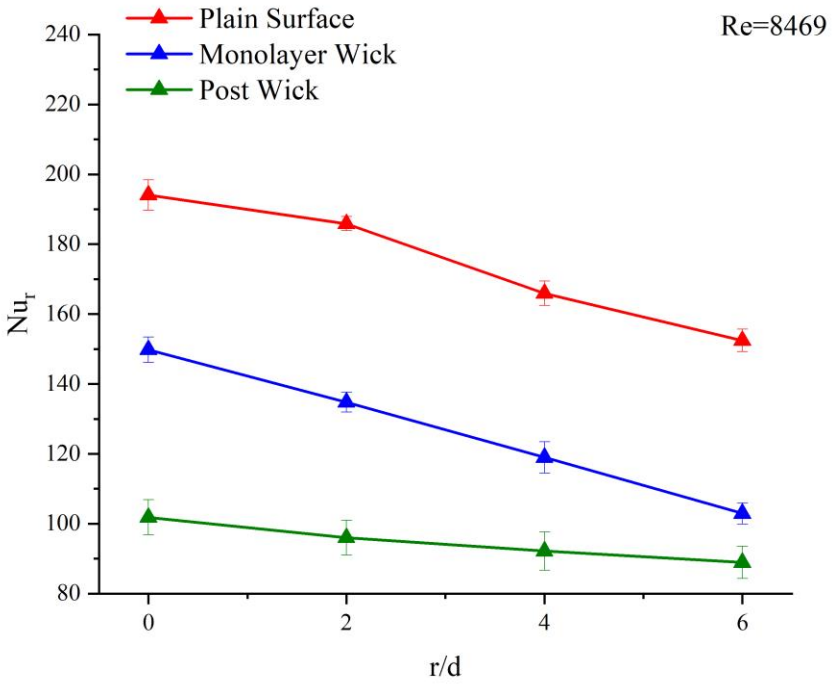

Figure 4.12: Nusselt Number vs. Lateral Variation for Re=8469 (Submerged).

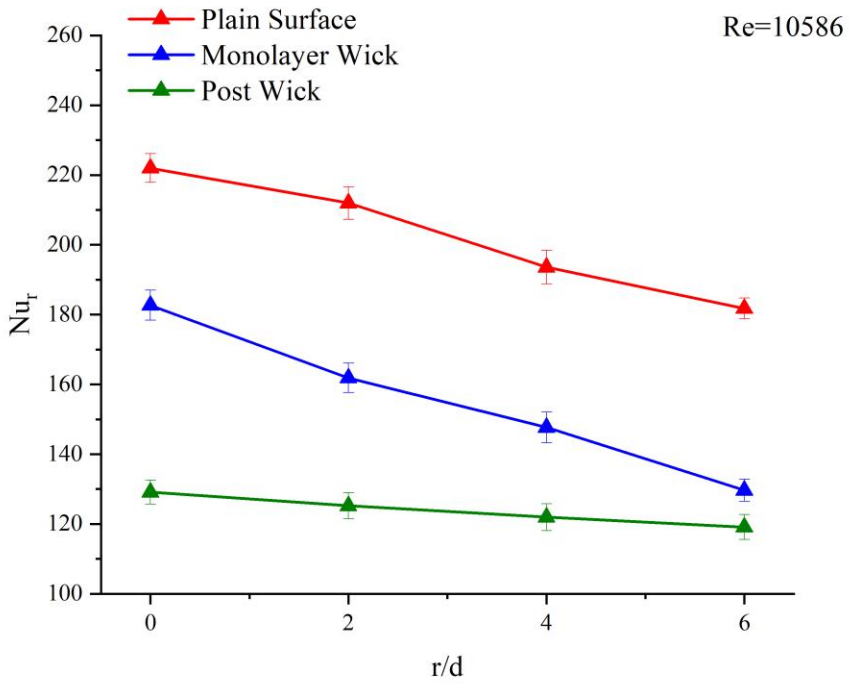

Figure 4.13: Nusselt Number vs. Lateral Variation for Re=10586 (Submerged).

4.2 Boiling Experiment

The goal of the boiling experiment was to see if an increase in CHF could be obtained. This was done by using porous mediums, in this case, the monolayer and columnar post wick and by also adding an impinging jet. Previous research has shown that by employing porous mediums to a boiling apparatus, there is an increase in the CHF and HTC [4]. Specifically, the monolayer wick reduces the superheat by reducing the effective thermal conduction path. Similarly, the columnar post wick actively modulates the hydrodynamic instability wavelength to increase the CHF.

To see if a further increase in CHF could be obtained, an impinging jet was added to reduce the liquid-vapor phase change generation. Four different flow rates were used for this investigation. Table 4.2 summarizes the flow rates and the calculated Reynolds numbers. It is seen in Table 4.2 that there is a flow rate of zero. This indicates that no impinging jet was used, and natural pool boiling occurred. Also, looking at Table 4.2, all Reynolds numbers are less than the 2,300 threshold for turbulent flow, meaning only laminar flow was used for the boiling experiment. This was done to allow bubble generation during the boiling phenomenon but also not to cause too much of a disturbance. All three surfaces were analyzed with a goal in mind of determining the behavior under an impinging jet.

Table 4.2: Flow Rates for Boiling Experiment with Corresponding Reynolds Number.

Flow Rate (cc/min)	Reynolds Number
0	0
40	846
60	1270
80	1693

4.2.1 Boiling Validation

As with the non-boiling experiment, the boiling experiment needed to be validated to make sure a working apparatus was correctly fabricated and to ensure accurate results. The validation was done under no impinging jet, just a basic pool boiling setup. The correlation used for the boiling validation consisted of the correlation conducted by Warren M. Rohsenow [2,5,6]. Equation 4.6 shows the Rohsenow correlation. It should be noted that the condition of the heater surface has an influence on the heat transfer effects. Hence, the Rohsenow correlation is only applicable to a clean and polished surface. For the heat transfer rate for a given excess temperature and for the excess temperature for a given heat transfer rate, the Rohsenow equation's values can be off by ±100% and ±30%, respectively. Hence careful consideration was used with this correlation. It is seen in Equation 4.6 that multiple factors play a role in nucleate boiling. Most of these values are obtained through property values and are easily tabulated in heat transfer textbooks. Figure 4.14 shows the empirical correlation of Rohsenow plotted against the present study.

$$\dot{q}_{nucleate} = \mu_l h_{fg} \left[\frac{g(\rho_l - \rho_v)}{\sigma}\right]^{0.5} \left[\frac{c_{pl}(T_s - T_{sat})}{C_{sf} h_{fg} Pr_l^n}\right]^3 \quad 4.6$$

The Rohsenow correlation was plotted with ±20% uncertainty to allow for experimental error in the present study. It is seen in Figure 4.9 that the present study suites the correlation well with little variation in the present study. Error bars are present for the ΔT_{excess} measurements. This is due to the measurements in the surface temperature needed to calculate ΔT_{excess}. All errors calculated were less than 5%. This validation presents the validity needed to continue the boiling experiment and compare the plain surface to the two different porous media plates.

Careful consideration was taken into account around the CHF point. For water boiling at 1 atm of pressure, CHF is obtained around a ΔT_{excess} of ~30°C. This CHF phenomenon happens when the rate of evaporation at the heater surface reaches high values. These high values of evaporation results in surface dry-out. Surface dry-out prevents the liquid from reaching the boiling surface, which could result in a rapid temperature increase. During experimentation, this surface dry-out was carefully monitored so that damage would not occur to the heater apparatus.

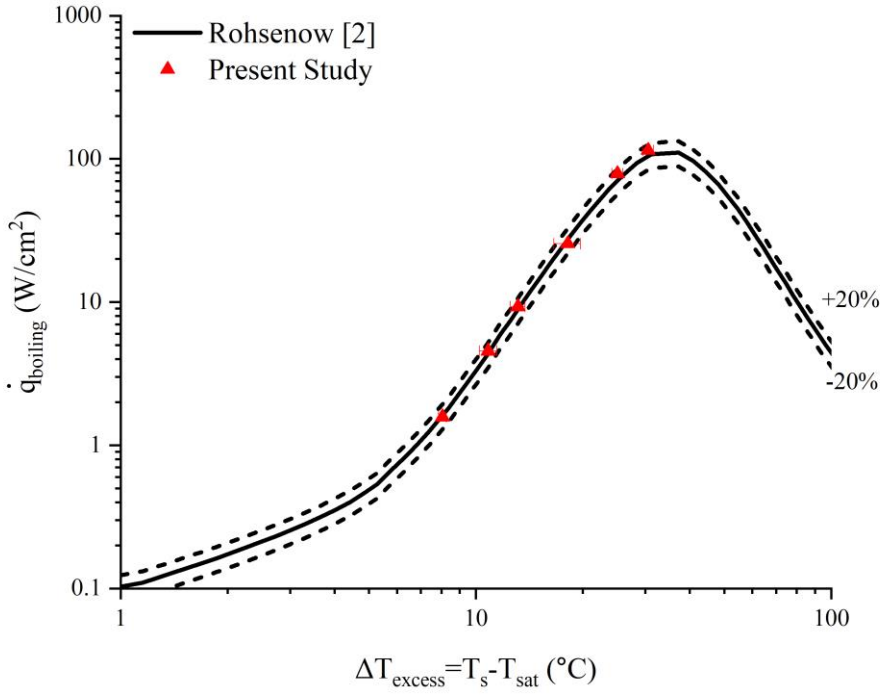

Figure 4.14: Experimental Boiling Validation.

4.2.2 Boiling Results

As stated previously, the boiling results used a total of four different flow rates, including zero. The zero flow rate was done to mimic a basic pool boiling experiment and to compare the porous media to previous research. Figure 4.15 shows the pool boiling effect on all different plate types with and without an impinging jet. First, a comparison was done to see how the different plates vary from each other, with an impinging jet and without. The results plotted were of a typical boiling curve measuring the applied heat flux and ΔT_{excess}. Figure 4.16 through Figure 4.19 show the comparison of the different plates undergoing pool boiling and subjected to an impinging jet.

Looking at a Reynolds number of zero, no impinging jet, the columnar post wick developed the highest CHF. With a pitch distance l_p=1 mm, the ΔT_{excess} is significantly reduced, allowing for a gradual increase in heat flux. Though the columnar post wick has the thickest wick structure, which is expected to increase the ΔT_{excess} through a larger conduction resistance, this is not the case. The modulation of the columnar post-wick structure allows for a significant decrease in the ΔT_{excess}. The reduction in ΔT_{excess} via the monolayer wick happens by the thin layer of copper sinter particles. This is due to an increase in the HTC, which is directly related to the increased effective thermal conductivity. The CHF enhancements of both monolayer wick and columnar post wick are related to the decrease in the hydrodynamic instability wavelength. This means a finer bubble generation reducing the vapor generation and prohibiting surface dry-out. This dry-out is present in the plain surface. The polished surface of the plain surface allows for a greater hydrodynamic instability wavelength which increases the vapor generation and causes rapid boiling.

When adding an impinging jet to the boiling experiment, the CHF is higher for all plates. For the plain surface, by adding an impinging jet, the flow impinges the boiling surface disrupting bubble generation. By disrupting bubble generation, the vapor phase is reduced, preventing surface dry-out. By avoiding this surface dry-out, the CHF was increased. By the reduced hydrodynamic instability wavelength of both the monolayer wick and columnar post wick having an influence on the increase of CHF, the impinging jet added to this benefit. With finer bubble generation in the monolayer wick and columnar post wick, the impinging jet was able to sweep the bubble generation away, again reducing the vapor phase of the boiling phenomenon. The combination of these two influences produced a higher CHF.

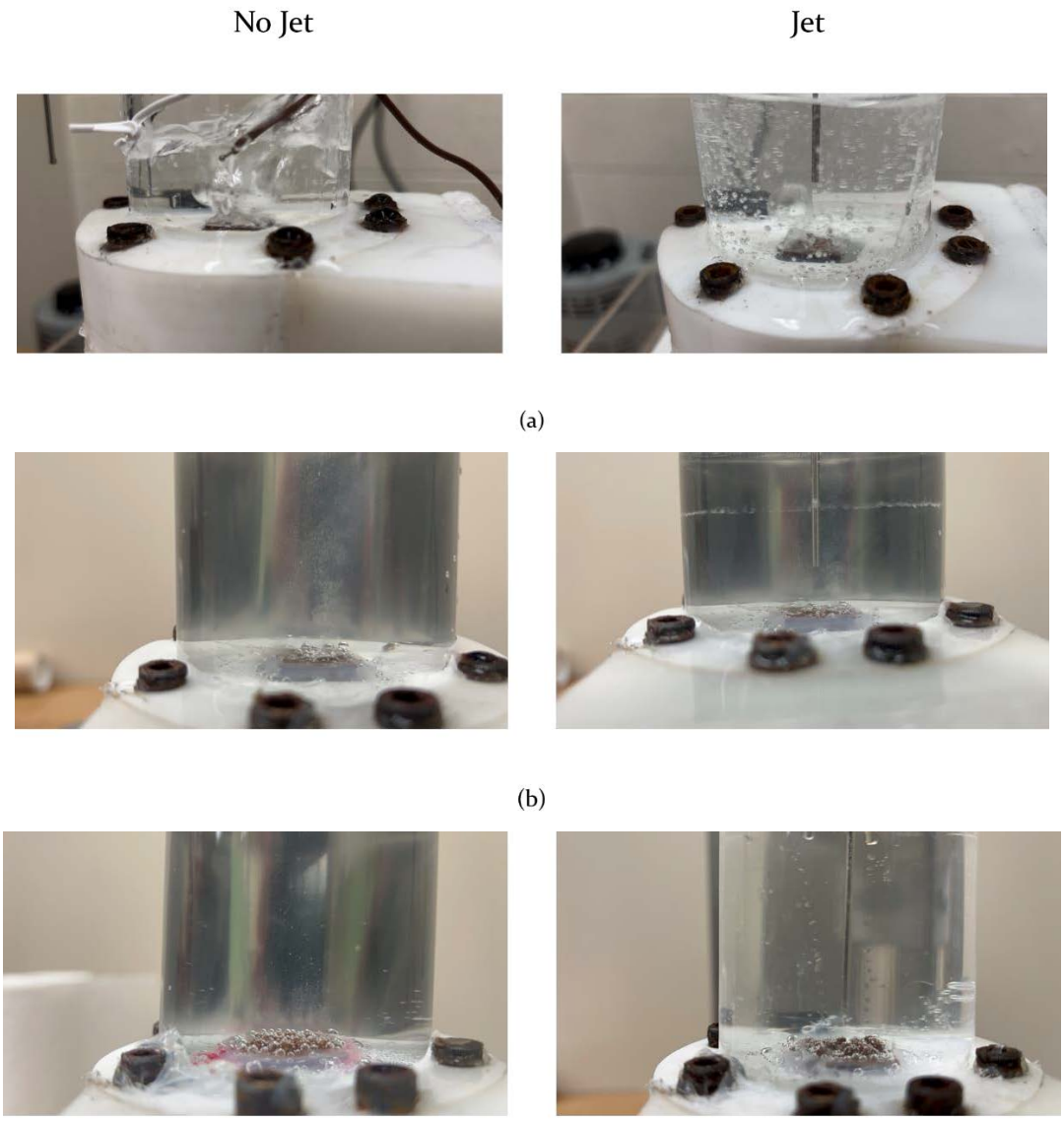

Figure 4.15: Pool Boiling with No Jet and Jet (a) Plain Surface, (b) Monolayer Wick, (c) Columnar Post Wick.

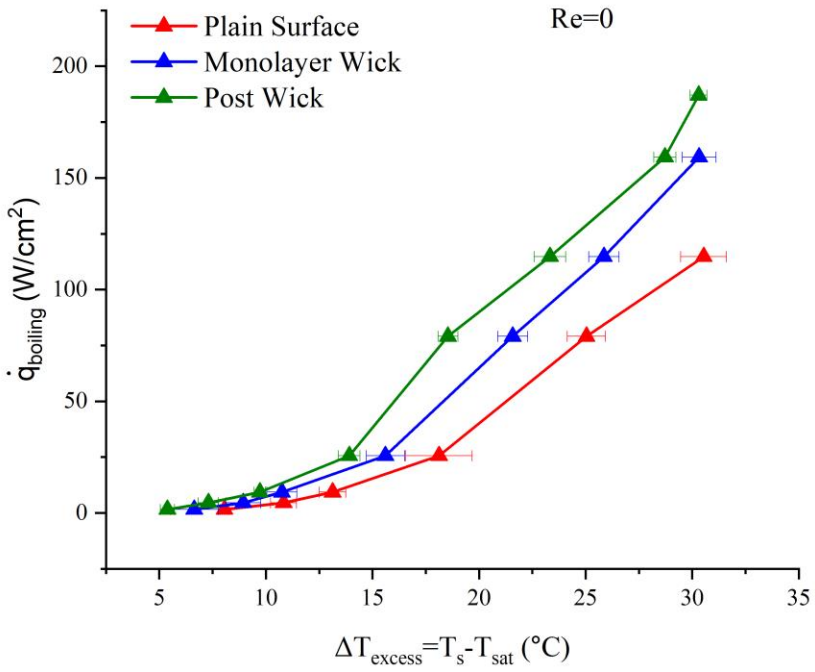

Figure 4.16: Boiling Curves for Re=0.

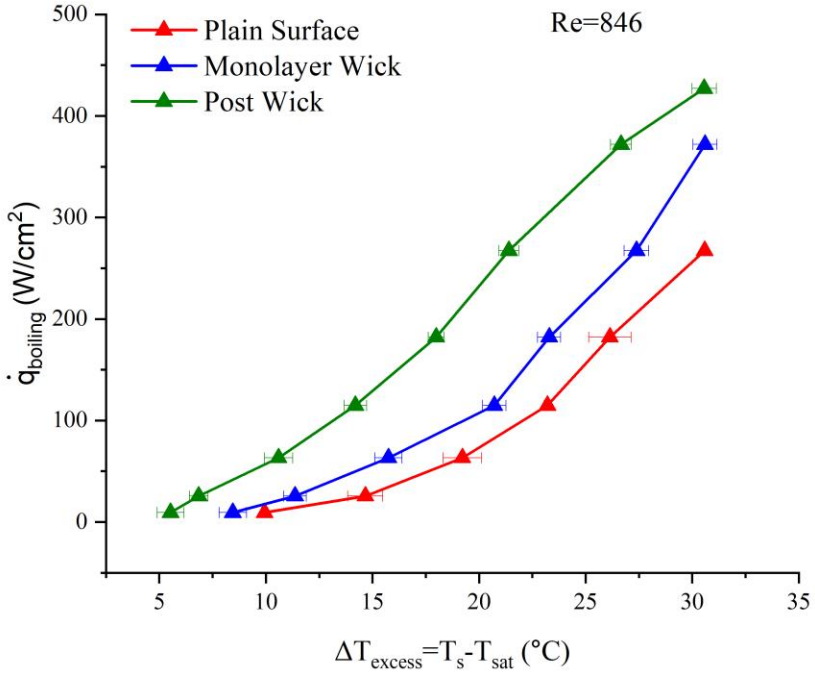

Figure 4.17: Boiling Curves for Re=846.

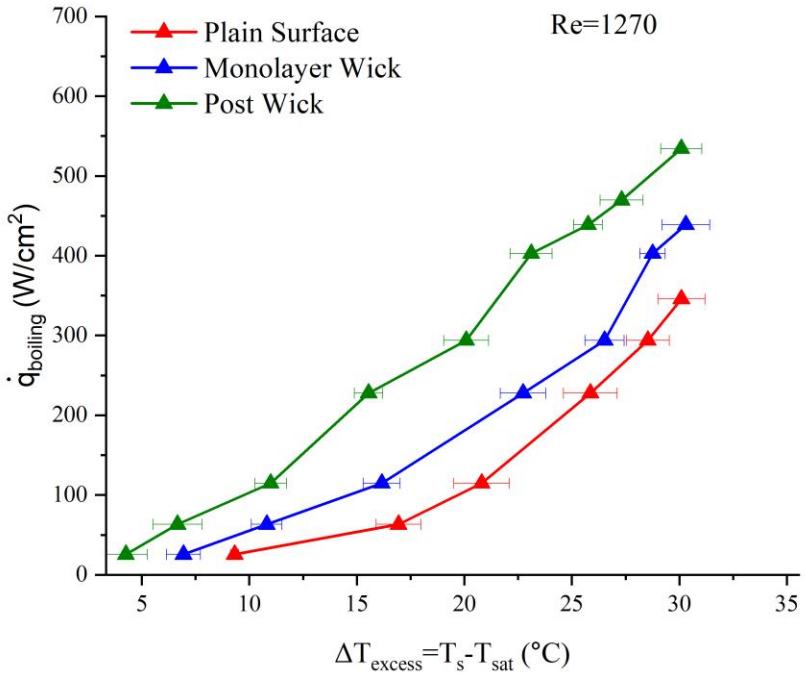

Figure 4.18: Boiling Curves for Re=1270.

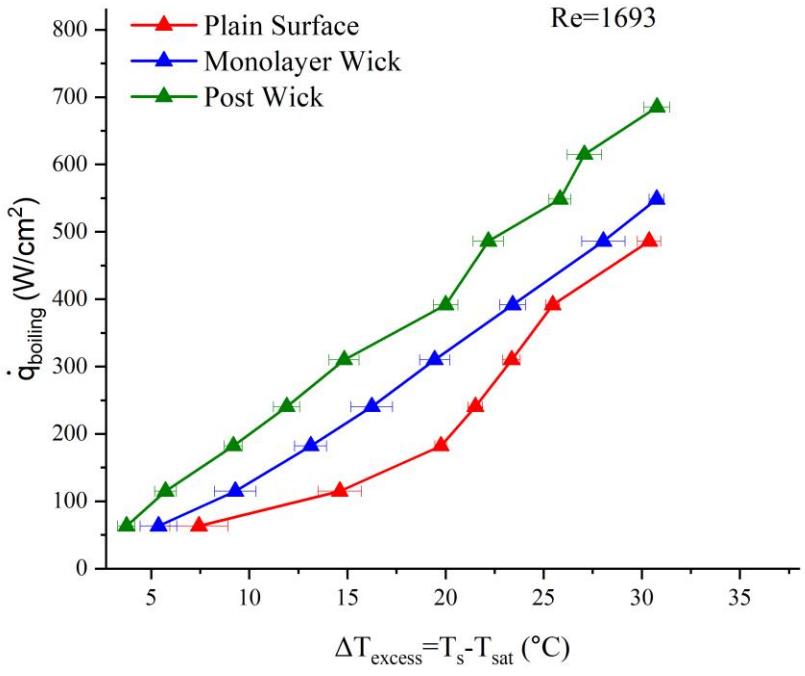

Figure 4.19: Boiling Curves for Re=1693.

The final results analyzed was the Reynolds number influence on the critical heat flux for each individual plate. Figure 4.20 through Figure 4.22 show the Reynolds number influence during boiling for each individual plate. It is seen in the figures that the Reynolds number has a significant influence on the CHF during boiling. Looking at the plain surface, by adding an impinging jet and increasing the flow rate, the CHF is further increased. This is due to the increase in fluid contact with the impinging surface and reducing the vapor phase. By reducing the vapor phase of boiling, the impinging jet reduces surface dry-out of the impinging surface. By reducing the chance for surface dry-out, the ΔT_{excess} is reduced, which further increases the CHF by keeping fluid contact with the impinging surface.

For the monolayer wick, its CHF increase is influenced by the decrease in the hydrodynamic instability wavelength, which reduces the size of vapor generation, i.e., smaller bubble generation. The other influence in increased CHF is the reduction of ΔT_{excess} at a given heat flux input by increasing the HTC, which is related to the increased thermal conductivity of the monolayer wick. By adding an impinging jet to the monolayer wick, the CHF is further increased. This again has to do with the liquid vapor phase change during the boiling phenomenon. The impinging jet allows for more fluid contact with the surface, further increasing the CHF. The geometry of the monolayer wick and the impinging jet have major influences on the CHF increase of the monolayer wick.

Lastly, another major CHF enhancement is present with the columnar post wick with an added impinging jet. The first CHF enhancement from the columnar post wick comes from its geometry. With the pitch distance l_p set to 1 mm, the columnar post wick can actively control the hydrodynamic instability wavelength through the post pitch and to reduce the wick superheat. With the addition of the columnar post structure, the overall wick thickness is increased. This decreased the superheat through modulation. This allows the vapor to occupy the space among the post, and keep the vapor production between the post. By adding the impinging jet, the flow field is allowed to travel between those posts and sweep the bubble generation away. This reduces the vapor phase and allows for more fluid contact between the columnar post. Both the geometry of the columnar post wick and the added impinging jet have a big influence of the CHF enhancement. To summarize the values of the boiling experiment in detail, Table 4.3 and Table 4.4 show the percent increase in CHF enhancements.

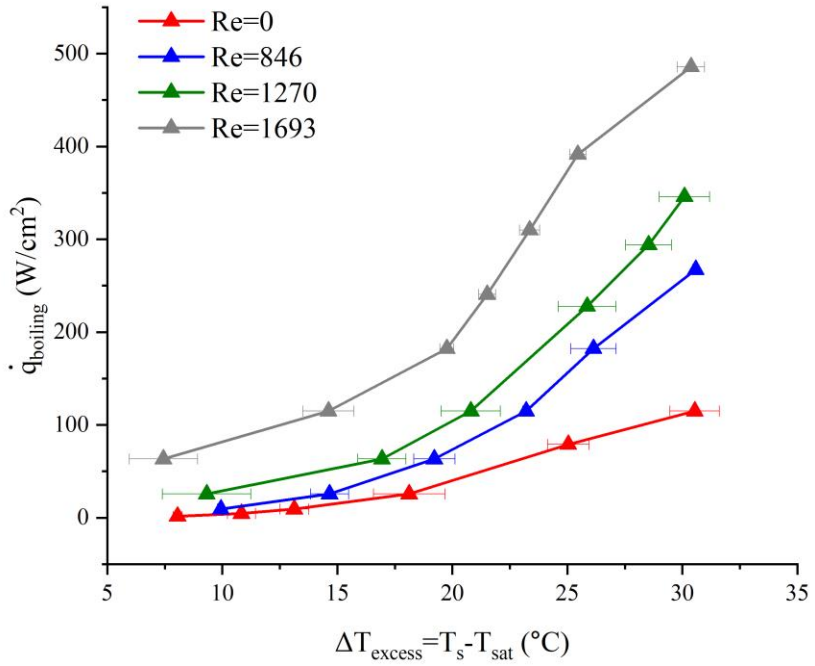

Figure 4.20: Effect of Reynolds Number on the Boiling Cure for the Plain Surface.

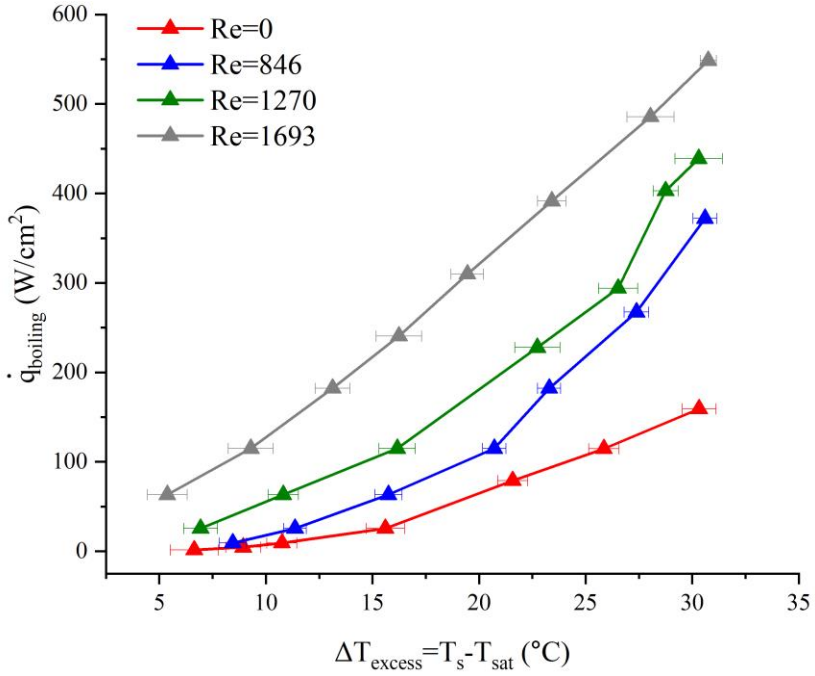

Figure 4.21: Effect of Reynolds Number on the Boiling Cure for the Monolayer Wick.

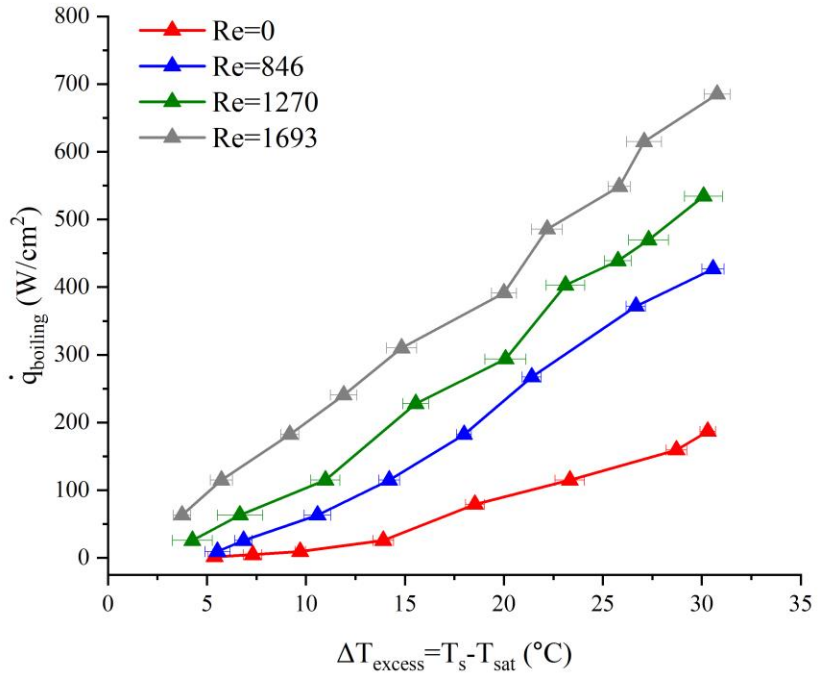

Figure 4.22: Effect of Reynolds Number on the Boiling Cure for the Columnar Post.

Table 4.3. CHF Enhancements When Compared to Plain Surface with No Jet.

When Compared To Plain Surface (No Jet)	
Monolayer Wick	Columnar Post Wick
39%	62.8%

Table 4.4. CHF Enhancements When Compared To Their Counterparts With No Jet.

Reynolds Number	When Compared To No Jet		
	Plain Surface	Monolayer Wick	Columnar Post Wick
846	132.80%	133.50%	128.40%
1270	201.30%	175.50%	185.92%
1693	323.10%	244.30%	266.60%

Chapter 5. Conclusions

5.1 Summary

The work done for this research led to two successfully conducted experiments. Those experiments being the non-boiling and boiling experiments. Though the outcomes of the experiments were not as expected, in some cases, the data collected from these experiments built on previous research and provided valuable information for future work.

1. The non-boiling experiment did not show the desired results. The validity of the free surface impinging jet apparatus did fall within ±10% of an empirical correlation of Webb and Ma [1]. Porous medium employment shows an increase in the HTC, which is typically demonstrated in heat exchangers and heat pipe apparatuses [32, 33, 43, 64-66]. However, this is not the case when it comes to impinging jets on porous surfaces. Results showed that the plain surface performs the best when compared to the monolayer wick and columnar post wick. Under a free surface jet, the velocity gradient is greater on the impinging surface. On the monolayer wick, the copper-sintered particles create a rough surface which increases the flow resistance on the impinging surface. This results in a lower velocity gradient across the impinging surface. Lastly, the columnar post wick shows the lowest free surface convection effect. The thick post wick fully disrupts the velocity gradient over the impinging surface and further increases the flow resistance.

2. For the submerged impinging jet case, the convection effect is greater for all three surfaces. This is due to complete fluid contact on the impinging surface. The validity of the submerged impinging jet apparatus also fell within ±10% of the submerged empirical correlation of Webb and Ma [1]. The plain surface still performed better when compared to the monolayer wick and columnar post wick. Again, flow resistance is the result of the lower convection faced with the monolayer wick and columnar post wick.

3. Change in the Nusselt number is present for all three plates during lateral nozzle variation. Moving away from the stagnation point shows a decrease in the Nusslt number for all plates and for both free surface and submerged jet experiments. Change in the Nusselt number is influenced by the hydraulic jump phenomenon in the free surface case. A high heat transfer rate is obtained inside the hydraulic jump due to the thin fluid film on the impinging surface [9]. Once the hydraulic jump moves away from the stagnation zone, the Nusselt number decreases. The lateral variation in the submerged case is present due to the wall jet, on exiting the nozzle. Variation on the change in the Nusselt number decreases in both monolayer wick and columnar post wick. Specifically, the variation in the Nusselt number is less on the columnar post wick due to the thick porous layer and the tight pitch distance.

4. The basic pool boiling experiment with no jet produced the desired results as expected. Furthermore, both the monolayer wick and the columnar post wick saw an increase in CHF [4]. Through experimentation, the plain surface reached a CHF of 114.8 W/cm^2 which falls within ±20% of the Rohsenow correlation [2,5,6]. For the monolayer wick, a CHF increase was obtained due to the uniform layer of copper-sintered particles. This improvement is connected to a potential reduction in the hydrodynamic instability wavelength when utilizing the uniform porous wick [7]. The monolayer wick obtained a CHF of 159.3 W/cm^2 which saw an increase of 39% in CHF enhancements when compared to the plain surface. The columnar post wick saw further CHF enhancements. By employing post structures, the columnar post wick is able to control the hydrodynamic instability wavelength through a post pitch of 1 mm and reduce the wick superheat [4,8]. The columnar post wick saw a CHF enhancement of 186.9 W/cm^2 which is a 62.8% increase when compared to the plain surface.

5. CHF enhancements were further increased when an impinging jet was added to the pool boiling setup. The plain surface, monolayer wick, and columnar post wick all saw CHF enhancements under a low flow rate impinging jet. By introducing an impinging jet to the pool boiling setup, more water contact is presented to the boiling surface. This water contact prevents surface dry-out, which results in a higher CHF. At the lowest flow rate, the plain surface, monolayer wick, and columnar post wick saw an increase of 132.8%, 133.5%, and 128.4%, respectively, in CHF enhancements when compared to the basic pool boiling setup. At the highest flow rate, the plain surface, monolayer wick, and columnar post wick saw an increase of 323.1%, 244.3%, and 266.6%, respectively, in CHF enhancements when compared to the basic pool boiling setup.

5.2 Future Work and Recommendations

Future research into impinging jets and pool boiling phenomena can be built on the findings of this study. For the non-boiling investigation, it would be interesting to see how the different porous media react to parallel flow rather than perpendicular flow. This could possibly reduce the flow resistance in the monolayer wick and columnar post wick that was present in the perpendicular flow. To increase the accuracy of the surface temperature measurements, a third thermocouple can be added to the heater apparatus, and this would allow for a non-linear extrapolation, further reducing the uncertainty in the surface temperature measurements. Instead of having three individual plates, fabrication of the different wick surfaces could be done a top of the impinging surface. This would eliminate the solder interface and would further increase the conductive path. A digital power supply would benefit the pool boiling experiment. Though the uncertainties would still be present, a digital reading would provide more accurate heat flux measurements. Other than copper-sintered particles making up the porous layer, other porous materials could be used, such as ceramic honeycomb structures. Adding an impinging jet to this material would provide beneficial research. Finally, increasing the size of the impinging surface would benefit for future research. This would allow more data for the lateral nozzle variation, which would be beneficial to draw more conclusions on the porous plates.

Bibliography

[1] B. W. Webb and C. F. Ma, "Single Phase Liquid Jet Impingement Heat Transfer," *Advances in Heat Transfer*, vol. 26, pp. 105–217, 1995.

[2] Y. A. Cengal and A. J. Ghajar, *Heat and Mass Transfer: Fundamentals & Applications*, 5th ed. New York, New York: McGraw Hill, 2015.

[3] Lienhard, J. H. V., Liu, X., and Gabour, L. A. (1992). Splattering and heat transfer during impingement of a turbulent liquid jet. J. Hear Transfer 114, 362-372.

[4] Y. Nasersharifi, M. Kaviany, and G. Hwang, "Pool-boiling enhancement using multilevel modulated wick," *Applied Thermal Engineering*, vol. 137, pp. 268–276, Mar. 2018.

[5] W.M Rohsenow, A method of correlating heat transfer data for surface boiling of liquids, Trans. Am. Soc. Mech. Eng. 74 (1952) 969-975

[6] W.M. Rohsenow, P. Griffith, Correlation of maximum heat flux data for boiling of saturated liquids, Chem. Eng. Prog. 52 (1956) 47.

[7] G. S. Hwang and M. Kaviany, "Critical heat flux in thin, uniform particle coatings," International Journal of Heat and Mass Transfer, vol. 49, no. 5, pp. 844–849, Mar. 2006.

[8] S. G. Liter and M. Kaviany, "Pool-boiling CHF enhancement by modulated porous-layer coating: theory and experiment," International Journal of Heat and Mass Transfer, vol. 44, no. 22, pp. 4287–4311, Nov. 2001.

[9] B. K. Friedrich, A. W. Glaspell, and K. Choo, "The effect of volumetric quality on heat transfer and fluid flow characteristics of air-assistant jet impingement," International Journal of Heat and Mass Transfer, vol. 101, pp. 261–266, Oct. 2016.

[10] T. R. Thomas, "Extrapolation Errors in Thermal Contact Resistance Measurements," Journal of Heat Transfer, vol. 97, no. 2, pp. 305–307, 1975.

[11] J. Fourier, *The Analytical Theory of Heat*. London, 1878.

[12] M. G. Cooper, B. B. Mikic, and M. M. Yovanovich, "Thermal contact conductance," *International Journal of Heat and Mass Transfer*, vol. 12, no. 3, pp. 279–300, Mar. 1969.

[13] M. Bahrami, J. R. Culham, and M. M. Yovanovich, "Modeling Thermal Contact Resistance: A Scale Analysis Approach," *Journal of Heat Transfer*, vol. 126, pp. 896–905, Dec. 2004.

[14] P. J. Berenson, "Experiments on pool-boiling heat transfer," *International Journal of Heat and Mass Transfer*, vol. 5, no. 10, pp. 985–999, Oct. 1962.

[15] M. Tingle, "Four simple experiments with counter-intuitive results," *Royal Society of Chemistry*, 02-Feb-2018. [Online]. Available: https://edu.rsc.org/ideas/four-simple-experiments-with-counter-intuitive-results/3008604.article.

[16] J. Kim and J. F. Benton, "Highly subcooled pool boiling heat transfer at various gravity levels," *International Journal of Heat and Fluid Flow*, vol. 23, no. 4, pp. 467–508, Aug. 2002.

[17] C. D. Henry, J. Kim, B. Chamberlain, and T. G. Hartman, "Heater size and heater aspect ratio effects on subcooled pool boiling heat transfer in low-g," *Experimental Thermal and Fluid Sciences*, vol. 29, no. 7, pp. 773–782, Aug. 2005.

[18] I. L. Pioro, W. Rohsenow, and S. S. Doerffer, "Nucleate pool-boiling heat transfer. I: review of parametric effects of boiling surface," *International Journal of Heat and Mass Transfer*, vol. 47, no. 23, pp. 5033–5044, Nov. 2004.

[19] S. Nukiyama, "The maximum and minimum values of the heat Q transmitted from metal to boiling water under atmospheric pressure," *International Journal of Heat and Mass Transfer*, vol. 9, no. 12, pp. 1419–1433, Dec. 1966.

[20] S. S. Kutateladze, *Heat Transfer in Condensation and Boiling*. 1959.

[21] N. Zuber, "On the Stability of Boiling Heat Transfer," *Journal of Fluids Engineering*, vol. 80, no. 3, pp. 711–714, Apr. 1958.

[22] N. Zuber, "Nucleate boiling. The region of isolated bubbles and the similarity with natural convection," *International Journal of Heat and Mass Transfer*, vol. 6, no. 1, pp. 61–78, Jan. 1963.

[23] N. Zuber, *Hydrodynamic Aspects of Boiling Heat Transfer*. 1959.

[24] H. K. Forster and N. Zuber, "Dynamics of vapor bubbles and boiling heat transfer," *AlChE Journal*, vol. 1, no. 4, Dec. 1955.

[25] J. H. Lienhard, V. K. Dhir, and D. M. Riherd, "Peak Pool Boiling Heat-Flux Measurements of Finite Horizontal Flat Plates," *Journal of Heat Transfer*, vol. 95, no. 4, Nov. 1973.

[26] K. Sun and J. H. Lienhard, "The peak pool boiling heat flux on horizontal cylinders," *International Journal of Heat and Mass Transfer*, vol. 13, no. 9, Sep. 1970.

[27] P. J. Berenson, "Film-Boiling Heat Transfer From a Horizontal Surface," *Journal of Heat Transfer*, vol. 83, no. 3, Aug. 1961.

[28] L. A. Bromley, *Heat transfer in Stable film boiling*. 1948.

[29] B. Agostini, M. Fabbri, J. E. Park, L. Wojtan, J. R. Thome, and B. Michel, "State of the Art of High Heat Flux Cooling Technologies," *Heat Transfer Engineering*, vol. 28, no. 4, pp. 258–281, Mar. 2007.

[30] R. C. Chu, R. E. Simons, M. J. Ellsworth, R. R. Schmidt, and V. Cozzolino, "Review of cooling technologies for computer products," *IEEE Transactions on Device and Materials Reliability*, vol. 4, no. 4, pp. 568–585, Dec. 2004.

[31] I. Mudawar and T. M. Anderson, "Optimization of Enhanced Surfaces for High Flux Chip Cooling by Pool Boiling," *Journal of Electronic Packaging*, vol. 115, no. 1, Mar. 1993.

[32] Z. J. Zuo, M. T. North, and K. L. Wert, "High heat flux pipe mechanism for cooling of electronics," *IEEE Transactions on Components and Packaging Technologies*, vol. 24, no. 2, Jun. 2001.

[33] H. N. Chaudhry, B. R. Hughes, and S. A. Ghani, "A review of heat pipe systems for heat recovery and renewable energy applications," *Renewable and Sustainable Energy Reviews*, vol. 16, no. 4, pp. 2249–2259, May 2012.

[34] R.T. Lahey, F.J. Moody, S. American Nuclear, R. United States. Energy, A. Development, The Thermal Hydraulics of a Boiling Water Nuclear Reactor, The Society, [Hinsdale, Ill.], 1977.

[35] K. Ghaedi, A. Alhusseny, A. Nasser, and N. Al-Zurfi, *Computational Overview of Fluid Structure Interaction*. London, United Kingdom: IntechOpen, 2021.

[36] H. M. Kurihara and J. E. Myers, "The effects of superheat and surface roughness on boiling coefficients," *AlChE Journal*, vol. 6, no. 1, Mar. 1960.

[37] W. Nakayama, T. Daikoku, and T. Nakajima, "Effects of Pore Diameters and System Pressure on Saturated Pol Nucleate Boiling Heat Transfer from Porous Surfaces," *Journal of Heat Transfer*, vol. 104, no. 2, pp. 286–291, May 1982.

[38] R. L. Webb and N. Y. Kim, *Journal of Enhanced Heat Transfer*, 2005.

[39] J. Wang and I. Catton, "Enhanced evaporation heat transfer in triangular grooves covered with a thin fine porous layer," *Applied Thermal Engineering*, vol. 21, no. 17, pp. 1721–1737, Dec. 2001.

[40] S. W. Ahmad, T. G. Karayiannis, D. B. Kenning, and A. Luke, "Compound effect of EHD and surface roughness in pool boiling and CHF with R-123," *Applied Thermal Engineering*, vol. 31, no. 11, pp. 1994–2003, Aug. 2011.

[41] A. E. Bergles and M. C. Chyu, "Characteristics of Nucleate Pool Boiling From Porous Metallic Coatings," *Journal of Heat Transfer*, vol. 104, no. 2, pp. 279–285, May 1982.

[42] A. K. Das, P. K. Das, and P. Saha, "Performance of different structured surfaces in nucleate pool boiling," *Applied Thermal Engineering*, vol. 29, no. 17, pp. 3643–3653, Dec. 2009.

[43] C. M. Patil and S. G. Kandlikar, "Pool boiling enhancement through microporous coatings selectively electrodeposited on fin tops of microchannels," *International Journal of Heat and Mass Transfer*, vol. 79, pp. 816–828, Dec. 2014.

[44] N. K. Choon, A. Chakraborty, S. Aye, and W. Xiaolin, "New pool boiling data for water with copper-foam metal at sub-atmospheric pressures: Experiments and correlation," *Applied Thermal Engineering*, vol. 26, no. 11, pp. 1286–1290, Aug. 2006.

[45] L. W. Jin, K. C. Leong, and I. Pranoto, "Saturated pool boiling heat transfer from highly conductive graphite foams," *Applied Thermal Engineering*, vol. 31, no. 14, pp. 2685–2693, Oct. 2011.

[46] I. Pranoto, K. C. Leong, and L. W. Jin, "The role of graphite foam pore structure on saturated pool boiling enhancement," *Applied Thermal Engineering*, vol. 42, pp. 163–172, Sep. 2012.

[47] W. Nakayama, T. Daikoku, H. Kuwahara, and T. Nakajima, "Dynamic Model of Enhanced Boiling Heat Transfer on Porous Surfaces—Part I: Experimental Investigation," *Journal of Heat Transfer*, vol. 102, no. 3, pp. 445–450, Aug. 1980.

[48] J. P. O'Connor and S. M. You, "A Painting Technique to Enhance Pool Boiling Heat Transfer in Saturated FC-72," *Journal of Heat Transfer*, vol. 117, no. 2, pp. 387–393, May 1995.

[49] K. N. Rainey and S. M. You, "Pool Boiling Heat Transfer From Plain and Microporous, Square Pin-Finned Surfaces in Saturated FC-72," *Journal of Heat Transfer*, vol. 122, no. 3, pp. 509–516, Apr. 2000.

[50] A. M. Gheitaghy, H. Saffari, D. Ghasimi, and A. Ghasemi, "Effect of electrolyte temperature on porous electrodeposited copper for pool boiling enhancement," *Applied Thermal Engineering*, vol. 113, pp. 1097–1106, Feb. 2017.

[51] Y.-W. Lu and S. G. Kandlikar, "Nanoscale Surface Modification Techniques for Pool Boiling Enhancement—A Critical Review and Future Directions," *Heat Transfer Engineering*, vol. 32, no. 10, pp. 827–842, Sep. 2011.

[52] H. J. Cho, D. J. Preston, Y. Zhu, and E. N. Wang, "Nanoengineered materials for liquid–vapour phase-change heat transfer," *Nature Reviews Materials*, vol. 2, no. 2, Dec. 2016.

[53] N. S. Dhillon, J. Buongiorno, and K. K. Varanasi, "Critical heat flux maxima during boiling crisis on textured surfaces," *Nature Communications*, vol. 6, no. 1, Sep. 2015.

[54] X. Zheng and C. W. Park, "Experimental study of the sintered multi-walled carbon nanotube/copper microstructures for boiling heat transfer," *Applied Thermal Engineering*, vol. 86, pp. 14–26, Jul. 2015.

[55] R. Ranjan, S. V. Garimella, J. Y. Murthy, and K. Yazawa, "Assessment of Nanostructured Capillary Wicks for Passive Two-Phase Heat Transport," *Nanoscale and Microscale Thermophysical Engineering*, vol. 15, no. 3, pp. 179–194, Jul. 2011.

[56] J. Y. Chang and S. M. You, "Enhanced boiling heat transfer from microporous surfaces: effects of a coating composition and method," *International Journal of Heat and Mass Transfer*, vol. 40, no. 18, pp. 4449–4460, Nov. 1997.

[57] J. H. Kim, K. N. Rainey, S. M. You, and J. Y. Pak, "Mechanism of Nucleate Boiling Heat Transfer Enhancement From Microporous Surfaces in Saturated FC-72," *Journal of Heat Transfer*, vol. 124, no. 3, pp. 500–506, May 2002.

[58] Y. V. Polezhaev and S. A. Kovalev, "Modelling heat transfer with boiling on porous structures," *Thermal Engineering*, vol. 12, pp. 617–620, 1990.

[59] Z. G. Xu and C. Y. Zhao, "Enhanced boiling heat transfer by gradient porous metals in saturated pure water and surfactant solutions," *Applied Thermal Engineering*, vol. 100, pp. 68–77, May 2016.

[60] A. Jaikumar and S. G. Kandlikar, "Ultra-high pool boiling performance and effect of channel width with selectively coated open microchannels," *International Journal of Heat and Mass Transfer*, vol. 95, pp. 795–805, Apr. 2016.

[61] D. H. Min, G. S. Hwang, Y. Usta, O. N. Cora, M. Koc, and M. Kaviany, "2-D and 3-D modulated porous coatings for enhanced pool boiling," *International Journal of Heat and Mass Transfer*, vol. 52, no. 11–12, pp. 2607–2613, May 2009.

[62] Z. G. Qu, Z. G. Zu, C. Y. Zhao, and W. Q. Tao, “Experimental study of pool boiling heat transfer on horizontal metallic foam surface with crossing and single-directional V-shaped groove in saturated water,” *International Journal of Multiphase Flow*, vol. 41, pp. 44–55, Jan. 2012.

[63] L. Bai, L. Zhang, J. Guo, G. Lin, X. Bu, and D. Wen, “Evaporation/boiling heat transfer characteristics in an artery porous structure,” *Applied Thermal Engineering*, vol. 104, pp. 587–595, May 2016.

[64] G. S. Hwang, M. Kaviany, W. G. Anderson, and J. Zuo, “Modulated wick heat pipe,” *International Journal of Heat and Mass Transfer*, vol. 50, no. 7–8, pp. 1420–1434, Apr. 2007.

[65] G. S. Hwang, Y. Nam, E. Fleming, P. Dussinger, Y. S. Ju, and M. Kaviany, “Multi-artery heat pipe spreader: Experiment,” *International Journal of Heat and Mass Transfer*, vol. 53, no. 13–14, pp. 2662–2669, Jun. 2010.

[66] G. S. Hwang *et al.*, “Multi-artery heat-pipe spreader: Lateral liquid supply,” *International Journal of Heat and Mass Transfer*, vol. 54, no. 11–12, pp. 2334–2340, May 2011.

[67] V. Stoyanov, V. Nikolov, and M. M. Garcia. "Numerical study of heat transfer between impinging gas jets and solid surfaces." In IOP Conference Series: Materials Science and Engineering, vol. 618, no. 1, p. 012064. IOP Publishing, 2019.

[68] Y. E. Akansu, M. Sarioglu, K. Kuvvet, and T. Yavuz, “Flow field and heat transfer characteristics in an oblique slot jet impinging on a flat plate,” *International Communications in Heat and Mass Transfer*, vol. 35, no. 7, pp. 873–880, Aug. 2008.

[69] K. Choo and S. J. Kim, “Heat Transfer and Fluid Flow Characteristics of Nonboiling Two-Phase Flow in Microchannels,” *Journal of Heat Transfer*, vol. 133, no. 10, Aug. 2011.

[70] X. Liu and J. H. Lienhard, “The hydraulic jump in circular jet impingement and in other thin liquid films,” *Experiments in Fluids*, vol. 15, no. 2, pp. 108–116, Jul. 1993.

[71] K. Choo and S. J. Kim, "The influence of nozzle diameter on the circular hydraulic jump of liquid jet impingement" *Experimental Thermal and Fluid Science*, vol. 78, p. 370, Nov. 2016.

[72] A. W. Glaspell, V. J. Rouse, B. K. Friedrich, and K. Choo, "Heat transfer and hydrodynamics of air assisted free water jet impingement at low nozzle-to-surface distances," *International Journal of Heat and Mass Transfer*, vol. 132, pp. 138–142, Apr. 2019.

[73] A. M. Kuraan, S. I. Moldovan, and K. Choo, "Heat transfer and hydrodynamics of free water jet impingement at low nozzle-to-plate spacings," *International Journal of Heat and Mass Transfer*, vol. 108, pp. 2211–2216, May 2017.

[74] J. B. Baonga, H. Louahlia-Gualous, and M. Imbert, "Experimental study of the hydrodynamic and heat transfer of free liquid jet impinging a flat circular heated disk," *Applied Thermal Engineering*, vol. 26, pp. 1125–1138, Dec. 2006.

[75] K. Anand, "Study of Single, Axisymmetric Micro Jet Impingement Cooling," May 2010.

[76] K. Choo, B. K. Friedrich, A. W. Glaspell, and K. A. Schilling, "The influence of nozzle-to-plate spacing on heat transfer and fluid flow of submerged jet impingement," *International Journal of Heat and Mass Transfer*, vol. 97, pp. 66–69, Jun. 2016.

[77] V. Rouse, "Comparison of heat transfer and fluid flow characteristics between submerged and free surface jet impingement for two-phase flow," Youngstown State University, 2018.

[78] Q. Li, Y. Xuan, and F. Yu, "Experimental investigation of submerged single jet impingement using Cu–water nanofluid," *Applied Thermal Engineering*, vol. 36, pp. 426–433, Apr. 2012.

[79] A. R. A. Ali and I. Janajreh, "Numerical Simulation of Turbine Blade Cooling via Jet Impingement," *Energy Procedia*, vol. 75, pp. 3220–3229, Aug. 2015.

[80] C. Jiang, T. Han, Z. Gao, and C. Lee, "A review of impinging jets during rocket launching," *Progress in Aerospace Sciences*, vol. 109, pp. 1–22, Aug. 2019.

[81] A. Pavlova and M. Amitay, "Electronic Cooling Using Synthetic Jet Impingement," *Journal of Heat Transfer*, vol. 128, no. 9, pp. 897–907, Feb. 2006.

[82] EngineeringToolbox,"SpecificHeat of some Metals," *Engineeringtoolbox.com*, 2019.https://www.engineeringtoolbox.com/specific-heat-metals-d_152.html